Material extrusion additive manufacturing of zirconia: from filament characterisation to Weibull statistics

Rapid Prototyping J

Material extrusion additive manufacturing of zirconia: from filament characterisation to Weibull statistics

Journal:	*Rapid Prototyping Journal*
Manuscript ID	RPJ-10-2023-0374.R1
Manuscript Type:	Original Article
Keywords:	Additive manufacturing, Material extrusion, Ceramics, Weibull statistics, Fracture analysis

Material extrusion additive manufacturing of zirconia: from filament characterisation to Weibull statistics

Abstract

Purpose - This research aims to investigate the performance of filament-based Material Extrusion additive manufacturing (MEX), combined with debinding and sintering as a novel approach to manufacturing ceramic components.

Design/methodology/approach - A commercial ZrO_2 filament was selected and analysed by IR spectroscopy, rheology and thermo-gravimetry. The influence of the print parameters (layer thickness, flow rate multiplier, printing speed) and sintering cycle were investigated to define a suitable printing and sintering strategy. Biaxial flexure tests were applied on sintered discs realised with optimised printing strategies and the results were analysed via Weibull statistics to evaluate the mechanical properties of printed components. The hardness and thermal conductivity of sintered components were also tested.

Findings – Layer thickness and flow rate multiplier of the printing process were proved to have significant effect on the density of as-printed parts. Optimised samples display a sintered density > 99% of the theoretical density, 20% linear sintering shrinkage, a characteristic flexural strength of 871 MPa with a Weibull modulus of 4.9, a Vickers hardness of 12.90 ± 0.3 GPa and a thermal conductivity of 3.62 W/mK. Gyroids were printed for demonstration purposes.

Originality/value – This work is the first to apply biaxial flexure tests and Weibull statistics to additively manufactured MEX zirconia components, hence providing comparable results to other additive technologies. Moreover, fractography analysis builds the connection between printing defects and the fracture mechanism of bending. This study also provides guidelines for fabricating high density zirconia components with MEX.

Keywords: Additive manufacturing, Material extrusion, Ceramic, Weibull statistics, Fracture analysis

1. Introduction

Technical ceramics are widely applied in multiple domains, such as aerospace and electronics, as they are excellent thermal and electrical insulators. However, due to their low

fracture toughness, ceramic component manufacturing is a labour and cost intensive process. It mostly relies on near-net-shape techniques, such as uniaxial pressing and injection moulding, and it is limited in geometrical shape and has high mould investment costs. Additive Manufacturing (AM) can however overcome these limitations.

Different AM technologies have been launched to process ceramics. Selective laser melting (SLM) is capable of processing pure ceramic powder above the melting temperature. This approach allows direct manufacturing of ceramics with high density (approx. 100%) at the cost of high investment and required preheating to avoid thermal warping (Yves-Christian *et al.*, 2010). Selective laser sintering (SLS), as a similar but indirect approach, applies a composite powder composed of ceramic and a secondary component as the binder (e.g. polymer/inorganic compound), yet fine mixing of the composite powder remains the major barrier of SLS (Chen *et al.*, 2018). Two other prominent AM technologies for ceramics: stereolithography (SLA) and material jetting (MJ) both utilise UV-curable resin and confer high density and strength to the fabricated final components (Nakai *et al.*, 2021; Willems *et al.*, 2021; Zeng *et al.*, 2022). On the other hand, the drawbacks of using ceramic slurry in SLA and MJ consist in the environmental impact of the toxic photo resin and limited choice of materials (Gibson and Rosen, no date).

Among various AM technologies, filament-based Material Extrusion additive manufacturing (MEX) (ISO/ASTM 52900) is one of the most widely utilised technologies to produce polymeric parts, due to the limited hardware investment and user-friendly printer setup. Apart from polymer printing, MEX has expanded to fibre-reinforced polymers, metals, and ceramics (Chen *et al.*, 2019; Galantucci *et al.*, 2019).

A MEX filament for ceramic part production typically consists of 45-55 vol% nanometric ceramic powders with a binder system acting as the backbone, tackifier, and plasticiser. The ceramic filament is heated to 160 - 265 °C (Nötzel *et al.*, 2021) in the extruding nozzle to obtain a low-viscosity melt that can be extruded and deposited. The as-printed part (green part) is subjected to one thermal or multiple (catalytic or solvent + thermal) debinding steps to remove most of the binder system, leaving a porous ceramic part with low organic binder content, referred to as the brown part. The brown part is then thermally debound and sintered to obtain dense ceramic components (Ferraris *et al.*, 2016). Additional machining processes can be applied to the green or sintered objects to reach a higher accuracy and surface finish. The introduction of the binders in MEX drastically lowers the required investment cost for AM of

ceramic and reduces potential hazards for users by avoiding directly operating with nanoparticles. The necessary post processes are accompanied by a longer production period and energy consumption, nevertheless, MEX achieves good cost-effectiveness compared to other AM technologies

Research on MEX of ceramics is still in an early stage. The available reports typically focus on a particular aspect, such as feedstock development or manufacturing feasibility in a trial-and-error approach. As an example, Onagoruwa et al. conducted extensive research on the employable binders and their functions as backbone, elastomer, tackifier, and plasticiser, and applied a polypropylene-based feedstock to produce mullite, fused silica, and titanium oxide-based filament feedstocks (Onagoruwa, Bose and Bandyopadhyay, 2001). Nötzel et al. developed a alumina filament using polyvinyl butyral and polyethylene glycol as binders, and reached a sintered relative density of 98% (Nötzel and Hanemann, 2020). Cano et al. studied the effect of the applied infill pattern during MEX on the flexural strength of sintered zirconia parts via 3-point bending. The parts with alternating +/- 45° infill direction had a final density of 97% and a characteristic flexural strength of 500 MPa with a Weibull modulus of 6.5 (Cano *et al.*, 2020). However, the studies are very fragmented and typically focused on a particular step of the process or part performance.

This work systematically investigates the MEX process of ceramics along the entire process chain including feedstock inspection, printing optimisation, two-step debinding, sintering, and sintered components characterisation. A 3Y-TZP zirconia grade was selected and studied due to its high strength potential and phase transformation induced fracture toughness attributed to the 3 mol% yttria stabiliser content. The density, Vickers hardness, thermal conductivity, and biaxial strength of the sintered zirconia parts were characterised and accompanied by a detailed fracture analysis. For the first time, biaxial flexure test was adopted to assess the mechanical performance of MEX fabricated zirconia part. This research further demonstrates the capability of filament-based material extrusion additive manufacturing to manufacture ceramic parts of satisfactory mechanical performance at limited costs.

2. Materials and Methods

2.1 Feedstock Materials

A 3 mol% yttria-stabilised zirconia (3Y-TZP) filament with a diameter of 1.75 mm was purchased from 3DCeram Sinto Tiwari GmbH (Germany). Amongst the commercially available filaments, only solutions involving chemical and/or thermal debinding with low

toxicity were considered for the sake of low environmental impact and reduced hazard. The diameter distribution of the filament was inspected with a laser diameter gauge (DGK2015, Proton Products) to ensure accurate material feeding during printing. Fourier transformed infrared spectroscopy (FT/IR-4200, Jasco Co.), was used for the binder characterisation in the ATR mode with a resolution of 4 cm^{-1}. Several FT-IR-ATR measurements were done at arbitrary points on each sample, and an average spectrum was computed. Thermo-gravimetric analysis (TGA) and differential scanning calorimetry (DSC) were performed (SDT Q600, TA Instruments) on the filament at a constant heating rate of 10 °C/min up to 1000 °C in pure Ar gas (Liquid Argon > 99.998%, $O_2 \leq 1.5$ ppm, Nippon Gases NV) to assist defining suitable thermal debinding and sintering strategies.

Rheology parameters of the material in the green state were measured using a rotational rheometer (Haake Mars III, Thermo Scientific) in parallel plate geometry. Specifically, plates of 20 mm diameter were adopted, and experiments were conducted at 180 °C under controlled shear rate conditions between 1 and 300 s^{-1} to emulate the rheological conditions during printing and achieve adequate torque values. All measurements were repeated five times and were performed in air. No thermal degradation was detected during the tests. Under these experimental conditions, the morphology of the polymer suspension was stable, as verified before and after measurements. Cross-sections of the filament were inspected by optical microscopy (K6000, Keyence) and scanning electron microscopy (SEM, Vega3 LMH, Tescan).

2.2 3D Printing

Different from thermoplastics, printing was performed on a Prusa i3 MK3s particularly with direct drive configuration which stably feeds the brittle filament without breaking. To ensure smooth extrusion, 0.4 mm was selected as the nozzle diameter as it is over 10 times bigger than the particle size of the studied zirconia in this research. Besides, a hardened steel nozzle was used to avoid abrasion. Screening experiments were conducted to identify a suitable process window. Accordingly, the following print parameters were maintained constant during sample production: nozzle temperature 180 °C, bed temperature 60 °C, fan cooling on at 25% from the 5^{th} layer, strand width 0.4 mm, double contour, and 100% infill with alternating +/- 45° patterns; whereas a full factorial design of experiments (DoE, see Table I, 3 repetitions per experiments) was applied to investigate the main and interaction effects of the layer thickness, printing speed and flow rate multiplier on the green printed density of 10×10×5 mm^3 prismatic parts.

Table I: Full factorial design of experiments.

Factors	level 1	level 2	level 3
Printing speed (mm/s)	10	30	50
Layer thickness (mm)	0.1	0.2	0.3
Flow rate multiplier	90%	100%	110%

2.3 Post Processing

Post-processing, successively in the form of: i) solvent debinding, ii) thermal debinding, and iii) pressureless sintering was applied to selected printed samples, and combined with suitable print parameters towards the establishment of best-practice manufacturing strategies. Post-processing was developed based on the results of the TGA analyses, and dedicated tests conducted internally. Accordingly, the parts were immersed in a magnetically stirred acetone bath for 48 h during solvent debinding, at a temperature 40 °C to accelerate the process and avoid cracking. The solvent was replaced with fresh acetone after 24 h. Afterwards, the parts remained in open air for 12 h to allow evaporation of the residual acetone. The total weight loss after solvent debinding was 8.6%. The open porosity generated during binder dissolution allows a higher heating rate during the subsequent thermal debinding process, without the risk of cracking the part due to severe gas release.

Thermal debinding of the remaining binder occurred in a muffle furnace in air (Carbolite, model RHF 1200). The parts were initially heated to 150 °C at 1.3 °C/min and dwelled for 1 h. After that, the parts were heated from 150 °C to 450 °C with a heating rate of 0.5 °C/min and dwelled for 1 h. Cooling was performed at 5 °C/min to room temperature. The weight loss by thermal debinding was 5.7%. The applied solvent temperature, heating rates, dwelling times, and 2-step debinding strategy accomplished a good balance between process time and defect free parts (Thomas-vielma, Cervera and Levenfeld, 2008). Finally, the parts were sintered in air (Nabertherm HT16/17) by heating to 1000 °C at 4 °C/min and to 1475 °C at 2 °C/min with a dwell time of 2 h.

2.4 Characterisation

The Archimedes method (ISO 18754:2020) was selected to measure the actual volumetric density (g/cm^3) due to its high accuracy in comparison to cross-section microscopy and micro-CT. The density of the filament, as well as green and sintered parts was measured in ethanol using an analytical balance (Quintix 224-1S, Sartorius). Microstructural analyses were performed by Scanning Electron Microscopy (SEM, XL30FEG, FEI) on mirror-polished and

platinum-coated cross-sectioned sintered parts. Biaxial flexure test (ISO 6872:2015) was selected due to the larger sample volume tested in tension compared to 3-point bending testing and the available literature references for comparison (Miura *et al.*, 2020). Accordingly, two populations of 30 disc samples with a thickness of 1.2 mm and a diameter of 14 mm were manufactured with the best-practice manufacturing strategy for mechanical testing. A 20% disc oversize was set during printing to compensate for sintering shrinkage, grinding, and polishing, required during sample preparation. The biaxial flexure test were performed on an Instron 5567 with a crosshead speed of 1 mm/s. The strength data were analysed by Weibull statistics, allowing to quantify the characteristic strength, i.e. the strength at which 63.2% of the samples fracture, and the Weibull modulus, which quantifies the strength distribution. The fracture surfaces were characterised by SEM (nanoSEM, FEI) after gold coating. The Vickers hardness (H_V) of polished prismatic parts, produced by the best-practice manufacturing strategy, was measured (Model FV700, Future Tech Corp, Tokyo, Japan) using a load of 98 N applied for 10 s. Five indentations were made on each part. In addition, thermal conductivity at room temperature was measured on cylinders (D24.3 mm × 2.1 mm) of one of the best-practice manufacturing strategies, using a Modified Transient Plane Source (MTPS) (ASTM D7984) single-sided sensor (Trident, C-Therm Technologies Ltd, Fredericton, Canada). Complex gyroids were manufactured for demonstrative purposes.

3. Experimental results and discussion

3.1 Feedstock Characterisation

The as-supplied filament diameter was measured to be 1.753 ± 0.004 mm. Correspondingly, the measured distribution (given in Figure 1a) forms a nearly normal distribution with $\sigma = 0.0042$ and $\mu = 1.753$. The high accuracy of the filament allowed for not only a stable material flow into the extruder, but also continuous friction between the feeding rollers and the

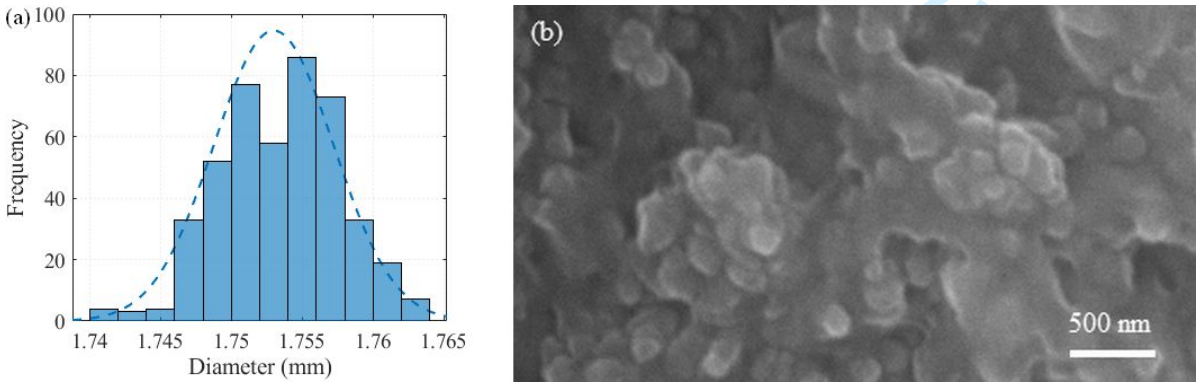

Figure 1: (a) Histogram of the measured diameter distribution of the zirconia filament; (b) SEM picture of a cross-sectional area of the zirconia filament.

filament creating constant pressure inside the nozzle. SEM inspection of cross-sections of the filament reveals zirconia particles in the nanometre range (Figure 1b).

The absorbance FT-IR spectrum of the zirconia-based filament shows prominent peaks at 2912 and 2848 cm^{-1} which allowed to identify polyethylene as the primary polymer in the filament (Figure 2). An additional peak was associated with primary aliphatic amine at 3397 cm^{-1}. The characteristic peaks of the zirconia particles were located in the 900 and 500 cm^{-1} range (Patel *et al.*, 2017). Based on the TGA results (Figure 3 (a)), a total weight loss of 14.49% was measured, indicating a powder load of 85.51 wt.% in the feedstock, equivalent to 50 vol.% given the average density of polymeric binders. Moreover, the presence of three types of binders in different proportions can be distinguished with onset decomposition temperatures of 170 °C, 385 °C, and > 500 °C, respectively. An endothermic peak at 55.1 °C in the DSC curve (Figure 3a) indicates the melting process of a binder, which is believed to be paraffin wax (Giavarini, C. Pochetti, 1973; Jayalakshmi *et al.*, 2007; Nötzel and Hanemann, 2020). Most of the weight loss occurs in the range of 150 °C - 450 °C, which is later defined as the temperature for thermal debinding. The total weight loss of 14.49% equals the one registered after solvent and thermal debinding (see sect. 2.3).

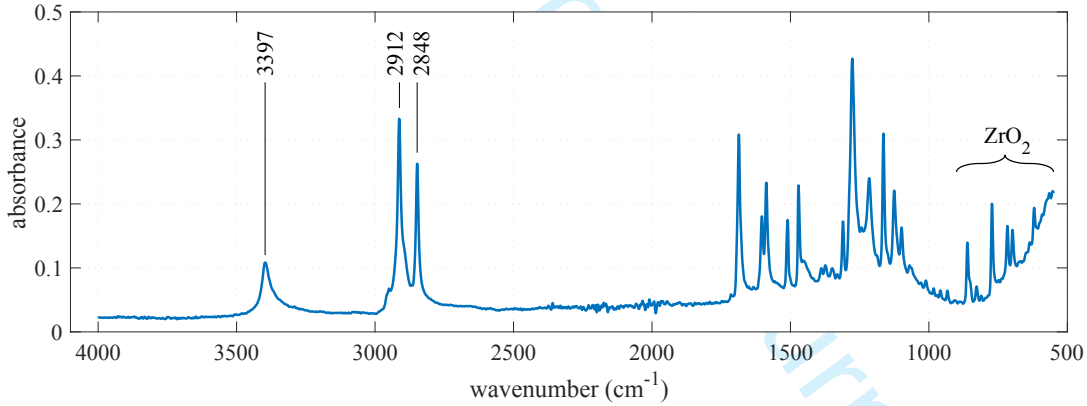

Figure 2: FT-IR spectrum of the as-purchased zirconia filament.

According to the rheological data (Figure 3b), the viscosity rapidly drops eight orders of magnitude from the lowest to the highest shear regime, reaching an infinite-shear viscosity of 5×10^{-4} Pa·s at 102 s^{-1}, which corresponds to the shear rate applied during printing (shear rates under printing > 102 s^{-1}). When compared with typical MEX filament polymeric data (in-house measurements and literature data (Spina, 2019)), this infinite-shear viscosity is particularly low, most likely due to the proper binder system allowing to well-disperse the nanometric zirconia particles.

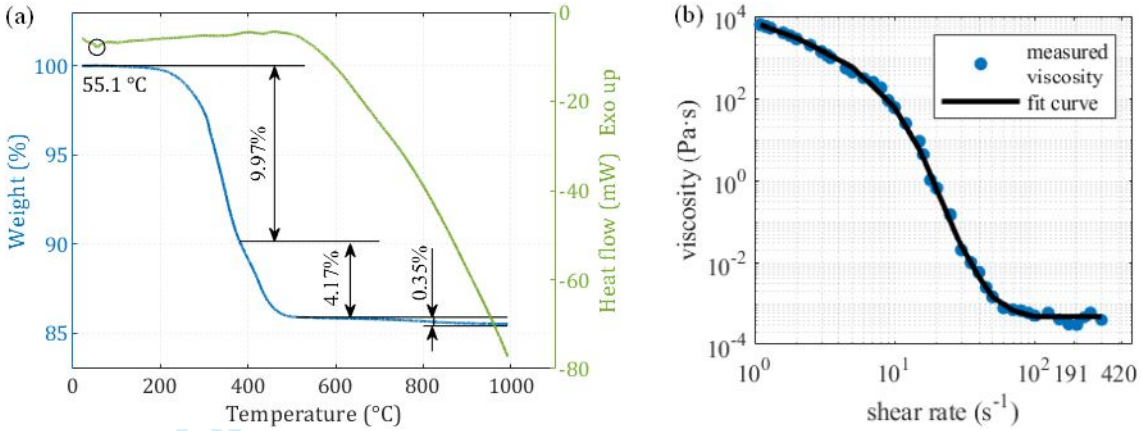

Figure 3: (a) TGA (blue) and DSC (green) curve of the zirconia filament; (b) viscosity of the feedstock melt at 180 °C as a function of shear rate and its spline fit curve.

3.2 3D Printing

Figure 4 provides a colour map of the relative green density of ZrO_2 printed samples as a function of the flow rate multiplier and layer thickness for a representative printing speed of 30 mm/s. An increase in the flow rate multiplier and a decrease of the layer thickness favour high density printed parts; and relative green densities > 98% are easily achievable with a flow rate multiplier > 100%, regardless of the other parameters. The Analysis of variance (ANOVA) was utilised to analyse the effect of each tested printing parameter and their interactions on the green density. Accordingly, the green density data were tested against the F-distribution, and the corresponding p-values (that is the area under the F-distribution from the given F-values to the end of the distribution tail) were calculated. Notably, a p-value below the widely accepted benchmark of 0.05 indicates that the associated factor has a significant effect on the target parameter of the ANOVA (Sthle and Wold, 1989). Statistically, the flow rate multiplier is the most significant factor, followed by the layer thickness and their interaction, while the significance of the printing speed is negligible (Table II). The regression model's coefficient (R^2) is 0.91. Those identified trends well agree with the general understanding of the MEX process using filament feedstock. A high flow rate multiplier induces over-extrusion of material, which is beneficial to fill the gaps of printing, especially in the case of low viscous melts. This contribution is even more important when printing with high layer thickness (or more properly with layer thickness closer to the nozzle diameter) because of the larger porosity of the printed part as a result of the deposition of strands with almost circular cross sections. On the contrary, a lower layer thickness as compared to the nozzle diameter is, to a certain extent, in favour of a flat strand deposition, with almost rectangular cross-sectional profiles, which minimises the

gap across adjacent strands and overlapping layers, hence the printed part porosity (Serdeczny *et al.*, 2018). The negligibility of the printing speed can also be attributed to the low viscosity of the feedstock used.

Table II: Results of the Analysis of Variance (ANOVA) of the effect of printing factors on the green part densities.

Source	**Sum Sq.**	***p*-value**
Layer thickness	0.02892	2.83×1^{-6}
Printing speed	0.00156	4.30×10^{-1}
Flow rate multiplier	0.43473	8.41×10^{-30}
Layer thickness * printing speed	0.00485	2.70×10^{-1}
Layer thickness * flow rate multiplier	0.03315	7.87×10^{-6}
Printing speed * flow rate multiplier	0.00286	5.42×10^{-1}
Error	0.05669	
Total	0.56726	

The prismatic samples printed at 30 mm/s were then selected for post-printing processing via solvent, thermal debinding, and sintering, as from the post-processing protocol described in sect.2. Accordingly, two best-practice manufacturing strategies, as summarised in

Table III, could be identified. They were characterised by a green relative density > 98% and a sintered relative density > 99%; and they were further applied for sample and biaxial flexural disc production. The physical and mechanical characteristics of the sintered samples are summarised in Table IV and further discussed in the next section.

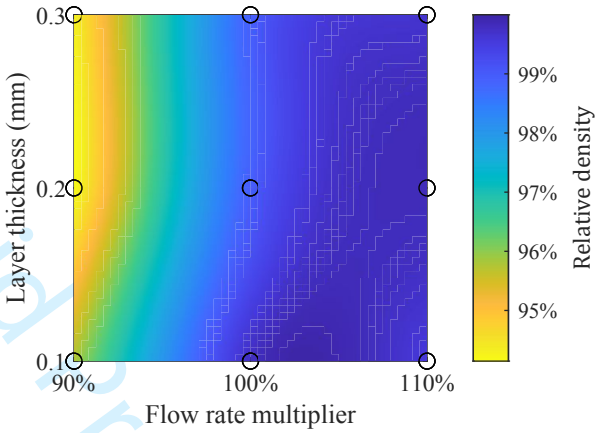

Figure 4: Color map of relative densities of zirconia printed green samples as a function of flow rate multiplier and layer thickness at a representative printing speed of 30 mm/s (interpolated data). The circles represent the location of the experimental data points.

Table III: Best-practice manufacturing strategies.

	01_100_30	**02_110_30**
Layer thickness (mm)	0.1	0.2
Flow rate multiplier	100%	110%
Printing speed (mm/s)	30	30
Green relative density[2]	98.87±0.03%	98.84±0.02%
Sintered relative density[3]	99.99±0.14%	99.38±0.06%

[2]Normalised to the density of the zirconia filament, 3.55 g/cm^3

[3]Normalised to the theoretical density of zirconia (3Y-TZP), 6.05 g/cm^3 (Tong *et al.*, 2016)

3.3 Characterisation of Sintered Parts

Figure 5 shows BSE images of representative cross-sections of sintered prismatic parts realised via best-practice manufacturing strategies 01_100_30 (a) and 02_110_30 (b). As shown, the cross-sections reveal a nearly fully dense microstructure with few aligned and randomly distributed pores. Particularly, elongated and layer-aligned residual pores with a maximum length of 60 µm and 120 µm, were detected in the cross-sections of 01_100_30 and 02_110_30 parts, respectively. The presence of pores can either be attributed to the inhomogeneity of the material feedstock, the inclusion of air bubbles in the low viscous melt, or printing defects. The larger flaw size of the 02_110_30 samples can be related to the higher printing layer thickness resulting in a larger inter-strand space.

The measured Vickers hardness was similar for both manufacturing strategies, and showed good consistency with zirconia parts fabricated via conventionally sintering (Cokic *et al.*, 2020) and material jetting (Willems *et al.*, 2021), while the flexural strength was substantially different. Table IV listed the results on hardness, thermal and mechanical properties of zirconia in this study and other references. The discs printed with printing strategy 01_100_30 had a Weibull modulus of 2.66 and a characteristic strength of 730 MPa, whereas the 02_110_30 strategy resulted in a higher Weibull modulus of 4.91 and characteristic strength of 871 MPa. The Weibull plots of both populations are compared in Figure 6, along with characteristic pictures of two fractured discs. Low-strength discs typically broke in 2 parts, while discs with a strength above 1000 MPa broke in 5 or 6 parts. The higher Weibull modulus obtained with the 02_110_30 strategy should be ascribed to the double printing layer thickness applied, implying printing half the number of layers and a reduced probability of inducing printing defects in comparison to the 01_100_30 strategy. The obtained characteristic flexural strength is superior to 508 MPa for MEX with a different printing strategy (Cano *et al.*, 2020), and it is comparable to the reported 702 MPa for conventional ceramic processing (Cokic *et al.*, 2020)

and other additively manufacturing technologies, such as 741 MPa for stereolithography (Lu *et al.*, 2020) and 1061 MPa for material jetting (Willems *et al.*, 2021). However, the Weibull modulus remains modest compared to the above-mentioned studies which range from 6.5 to 16.3, most likely due to the higher intrinsic defect-inducing nature of the MEX process using filament feedstock.

Table IV: Mechanical and thermal characteristics of 3Y-TZP discs and samples realised with best-practice manufacturing strategies in this study and other references using the same grade of zirconia.

Manufacturing method	**MEX 01_100_30**	**MEX 02_110_30**	**MEX**	**Speed Sintering**	**SLA**	**Material Jetting**
Vickers hardness (GPa)	12.98±0.03	12.90±0.33	/	13.1	/	12.8
Weibull modulus	2.66	4.91	6.5	6.3	8.7	8.5
Characteristic strength (MPa)	730	871	508	702	741.8	1061
Thermal conductivity (W/mK)	/	3.62±0.08	/	/	/	/
Bending test	biaxial	biaxial	3-point	biaxial	3-point	biaxial
Source	this study	this study	(Cano *et al.*, 2020)	(Cokic *et al.*, 2020)	(Lu *et al.*, 2020)	(Willems *et al.*, 2021)

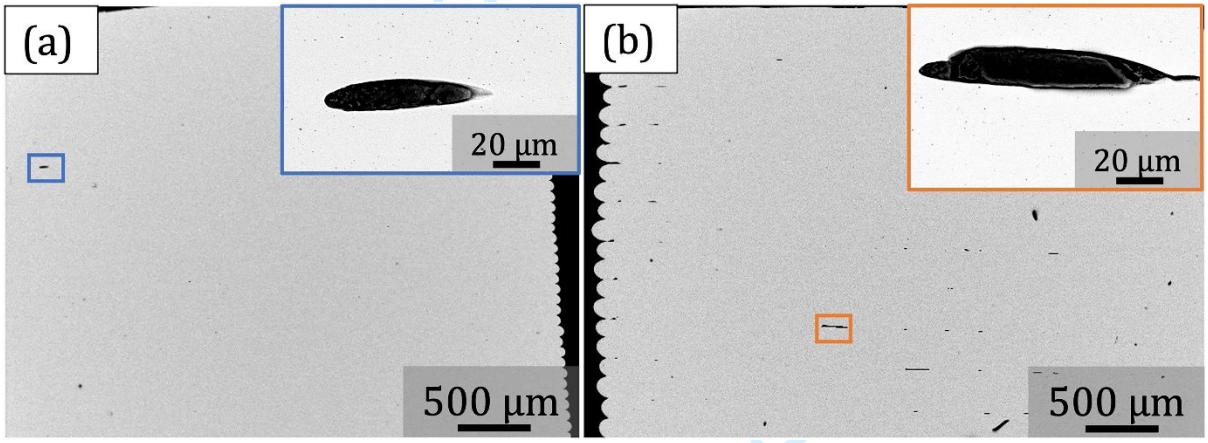

Figure 5: Backscattered Electron (BSE) images of representative cross-sections of sintered prismatic parts realised via best-practice manufacturing strategies 01_100_30 (a) and 02_110_30 (b).

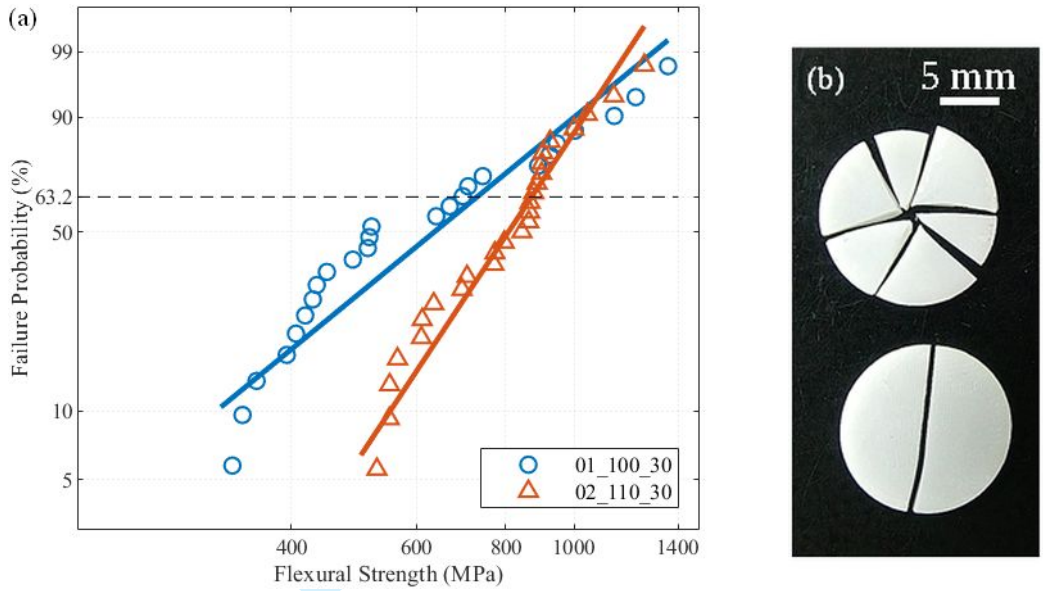

Figure 6: (a) Weibull plot of the biaxial flexural strength of 3Y-TZP discs (population 01_100_30 and 02_110_30) and (b) fractured discs after mechanical testing (right: bottom = low strength, top = high strength).

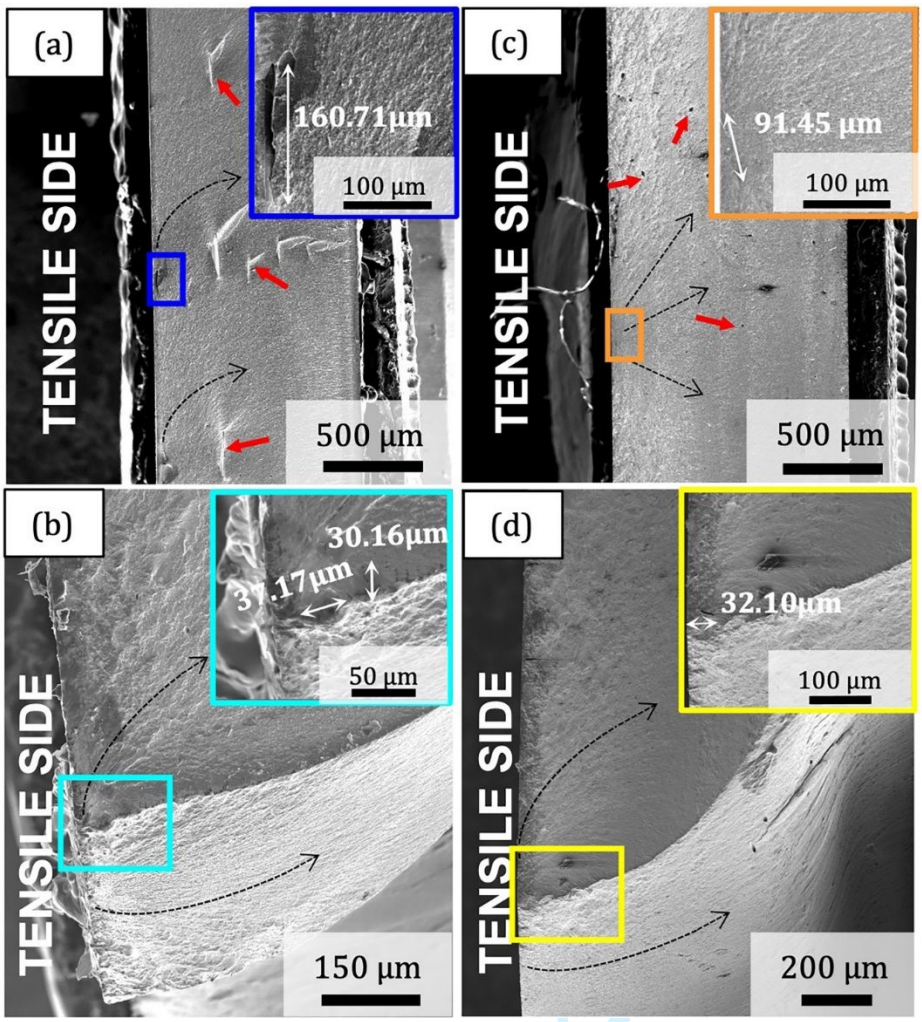

Figure 7: Secondary electron (SE) images of the biaxial fracture surface of 3Y-TZP discs manufactured by MEX using printing strategy 01 100 30 (a,b) and 02 110 30 (c,d). Indicative measurements of the critical flaw size.

The fractography analysis of a selection of biaxially fractured discs is shown in Figure 7. Two 01_100_30 discs with a flexural strength of 630 MPa (Figure 7a) and 1130 MPa (Figure 7b) and two 02_110_30 discs with the same flexural strength of 630 MPa (Figure 7c) and 1130 MPa (Figure 7d) were analysed. The dashed black arrows show the crack propagation direction observed on the fracture surface starting from the identified critical flaws. The crack initiation points were mainly investigated on the flat surfaces subjected to tensile stresses during testing where the crack propagation pattern appeared to originate from. For the low strength 01_100_30 part (Figure 7a), a possible crack initiation point was identified as an elongated void of ~160 µm in length and parallel to the printing direction as shown in the magnified

image (blue box in Figure 7a). Several defects with the same morphology (indicated by the red arrows) were observed over the complete fracture surface and were attributed to interlayer defects. On the contrary, for the low strength 02_110_30 part (Figure 7c), the critical flaw was identified as a smaller nearly spherical defect measured to be ~90 μm in diameter (as shown in the orange box in Figure 7c). Similar spherical isolated pores (pointed by the red arrows) were detected on the fracture surface as well. The significant variation in the morphology, size and amount of the voids between the low strength 01_100_30 and 02_110_30 parts did not account for any difference in their final strength. This discrepancy highlights that the position and orientation play a major role in the resulting mechanical properties compared to the percentage and distribution of defects. Despite the smaller size and aspect ratio of the porosity in the 02_110_30 part, the presence of a defect near the tensile surface determined the failure of the part at low stress values. On the other hand, being the orientation of the voids parallel to the tensile surface the 01_100_30 part resulted in the same value of strength. Since the part was tested in the favourable direction, the anisotropy generated through the layer-by-layer printing had a relatively limited impact on the mechanical properties in this case. For the high-strength parts, the fracture surface was analysed at low (Figure 7b-d) and high magnification (light blue and yellow box). The former highlighted the direction of the crack, whereas the latter enabled quantifying the size of the pores from which the crack initiated. In both cases, the critical defects are spherical in nature and of similar size. The formation of spherical pores could be correlated to air bubbles or ZrO_2 particle-free polymer agglomerates in the filament.

Strategy 02_110_30 was finally selected to fabricate cylinders for thermal characterisation too. The measured thermal conductivity was reported to be 3.62±0.08 W/mK at room temperature (Table IV), which is in good agreement with the reported value of 3.2 W/mK for conventionally pressed and sintered fully dense 3Y-TZP (Schlichting, Padture and Klemens, 2001), and slightly higher than the 2.99 W/mK reported for the same zirconia grade manufactured via stereolithography and sintered at 1600 °C (Liu *et al.*, 2023).

The printability and effect of the printing parameters were substantially related to the feedstock properties, such as binder properties, melt viscosity, particle size distribution, etc. A feedstock with comparable above-mentioned properties is essential to reproduce dense green parts using the printing strategy acquired in this study. Subsequently, the composite green parts underwent debinding and sintering and evolved into a monolithic ceramic. Similar conditions (temperature, heating ramp and dwelling time) as in this study or milder modifications of them facilitate defect-free binder removal and nearly full densification. In particular, the powder load

of the feedstock is a critical factor for densification during sintering. Using a filament with 43 vol.% powder, Guan et al. reported MEX fabricated zirconia with a relative density over of 99% after sintering, while an abrupt density drop occurred with a powder load below this threshold (Guan *et al.*, 2023). Therefore, a feedstock with a powder load above 43 vol.% (and ideally close to 50 vol.%) is regarded as a requirement to reproduce the results of this study.

3.4 Gyroid demonstrator

Gyroid parts (green size 30×30×7 mm^3) were printed as a benchmark piece demonstrating the shaping capability offered by the MEX technology (Figure 8). A linear sintering shrinkage of 18% was measured in X, Y and Z directions, which is in line with the level of shrinkage measured on the prismatic parts during the experimental campaign (19.89±0.62%). The shrinkage value is in good consistent with the linear shrinkage of ceramic via MEX and injection moulding in other researches - between 18% to 21% (Wright *et al.*, 1990; Cano *et al.*, 2020; Orlovská *et al.*, 2020; Nötzel *et al.*, 2021), and higher than the 5-11% via conventional firing (Correia, Hotza and Segadães, 2004). Defects like cracks, warpage or distortion were not observed on the sintered part, validating good geometry retention of the complex part containing overhanging and thin-wall structures during the sintering process. Hence, the isotropic linear shrinkage and fine geometry retention facilitate the application of this technology in industry.

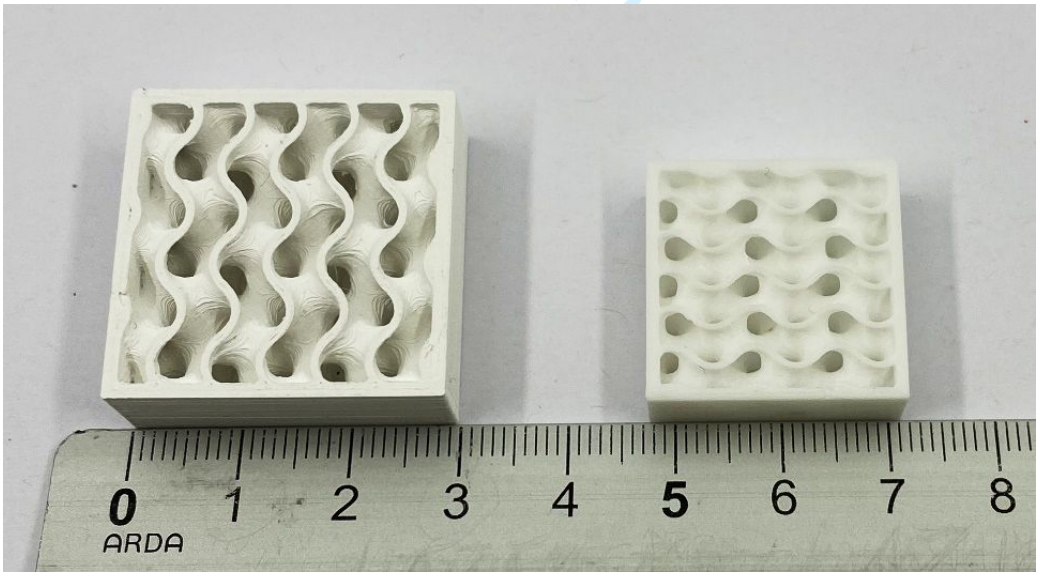

Figure 8: Green (left) and sintered (right) zirconia gyroid.

4. Conclusions

Material extrusion-based additive manufacturing using ceramic filament feedstock was proven to be capable of printing highly dense zirconia. Following conclusions were derived:

- DoE and ANOVA analyses of the printing parameters indicated that the layer thickness and flow rate multiplier significantly influence the as-printed green density. The printing strategy based on the statistical approach gave a sintered relative density >99%. This outcome can be extrapolated to other ceramic feedstocks with comparable particle size and morphology to fabricate dense parts via Material Extrusion with not only filament feedstock but also granulates, paste, etc..
- Satisfactory mechanical properties (Vickers hardness of 12.90 GPa, characteristic flexural strength up to 871 MPa and Weibull modulus of 4.9) were attained with the best-practice printing strategies. Analysis of the fractured surfaces revealed critical defects of variable size (indicatively in the range of 30 to 160 μm) of both spherical and elongated nature, attributed to inhomogeneities in the filament and inter-filament spacing printing defects, respectively.
- The sintered zirconia exhibited a thermal conductivity of 3.62 W/mK, a typical value for a dense 3Y-TZP ceramic, which is a thermal insulator.
- The sintered gyroid structure demonstrated homogeneous shrinkage and good geometry integrity after sintering. With the freedom of design due to additive manufacturing, zirconia serves as a good candidate for electrical and thermal insulation material.

The adoption of a commercially available filament introduced advantages in dimensional accuracy and printability. However, the unknown binder formulation forms a black box for processing. Under this circumstance, an exemplary strategy incorporating printing parameters, debinding conditions and sintering conditions was formulated in this study based on the extensive filament characterisation and the design of experiments on printing parameters to acquire defect-free zirconia components with high density and good mechanical properties. Details on the binder formulation would provide a reference from the material's perspective, which allows cross-validation between the experimentally formulated processing strategy of the whole process chain and the intrinsic property of the binders.

This study elucidates the impact of the printing parameters on the density of as-printed zirconia parts via Material Extrusion, and evaluated the mechanical and thermal properties of sintered specimens fabricated with the selected printing strategy. Future research will focus on the direct effect of printing strategy on mechanical property to further improve the reliability and strength of the material.

Acknowledgments

The authors acknowledge Frederik Desplentere for support in the filament diameter characterisation. The authors thank Prof. Luigi Galantucci of Politecnico di Bari for his precious suggestions and support. Part of this work is conducted in the framework of the SBO-FWO project Multi-Material Additive Manufacturing for Electrical Machines with increased performance (AM4EM, S001721N), funded by FWO-Vlaanderen.

References

Cano, S. *et al.* (2020) 'Influence of the infill orientation on the properties of zirconia parts produced by fused filament fabrication', *Materials*, 13(14). Available at: https://doi.org/10.3390/ma13143158.

Chen, A. *et al.* (2018) 'High-performance ceramic parts with complex shape prepared by selective laser sintering : a review', 6753. Available at: https://doi.org/10.1080/17436753.2017.1379586.

Chen, Z. *et al.* (2019) '3D printing of ceramics: A review', *Journal of the European Ceramic Society*, 39(4), pp. 661–687. Available at: https://doi.org/10.1016/j.jeurceramsoc.2018.11.013.

Cokic, S.M. *et al.* (2020) 'Mechanical properties, aging stability and translucency of speed-sintered zirconia for chairside restorations', *Dental Materials*, 36(7), pp. 959–972. Available at: https://doi.org/10.1016/j.dental.2020.04.026.

Correia, S.L., Hotza, D. and Segadães, A.M. (2004) 'Simultaneous optimization of linear firing shrinkage and water absorption of triaxial ceramic bodies using experiments design', *Ceramics International*, 30, pp. 917–922. Available at: https://doi.org/10.1016/j.ceramint.2003.10.013.

Ferraris, E. *et al.* (2016) 'Shaping of engineering ceramics by electro, chemical and physical processes', *CIRP Annals - Manufacturing Technology*, 65(2), pp. 761–784. Available at: https://doi.org/10.1016/j.cirp.2016.06.001.

Galantucci, L.M. *et al.* (2019) *Additive Manufacturing: New Trends in the 4th Industrial Revolution*, *Lecture Notes in Mechanical Engineering*. Springer International Publishing. Available at: https://doi.org/10.1007/978-3-030-18180-2_12.

Giavarini, C. Pochetti, F. (1973) 'Characterization of petroleum products by DSC analysis', *Journal of Thermal Analysis*, 5, pp. 83–94.

Gibson, I. and Rosen, D. (no date) *Additive Manufacturing Technologies*.

Guan, Z. *et al.* (2023) 'Additive manufacturing of zirconia ceramic by fused filament fabrication', *Ceramics International*, 49(17), pp. 27742–27749. Available at: https://doi.org/10.1016/j.ceramint.2023.05.230.

Jayalakshmi, V. *et al.* (2007) 'Characterisation of paraffin waxes by DSC and high temperature GC', *Petroleum Science and Technology*, 6466(May). Available at: https://doi.org/10.1080/10916469908949752.

Liu, Yansong *et al.* (2023) 'Influence of sintering temperature on the thermal conductivity of digital light processing 3D-printed yttria-stabilized zirconia ceramic', *Ceramics International*, 49(16), pp. 27514–27525. Available at: https://doi.org/10.1016/j.ceramint.2023.06.027.

Lu, Y. *et al.* (2020) 'Journal of the European Ceramic Society Flexural strength and Weibull analysis of Y-TZP fabricated by stereolithographic additive manufacturing and subtractive manufacturing', *Journal of the European Ceramic Society*, 40(3), pp. 826–834. Available at: https://doi.org/10.1016/j.jeurceramsoc.2019.10.058.

Miura, D. *et al.* (2020) 'Reliability of different bending test methods for dental press ceramics', *Materials*, 13(22), pp. 1–10. Available at: https://doi.org/10.3390/ma13225162.

Nakai, H. *et al.* (2021) 'Additively manufactured zirconia for dental applications', *Materials*, 14(13), pp. 1–9. Available at: https://doi.org/10.3390/ma14133694.

Nötzel, D. *et al.* (2021) 'Printing of zirconia parts via fused filament fabrication', *Materials*, 14(19). Available at: https://doi.org/10.3390/ma14195467.

Nötzel, D. and Hanemann, T. (2020) 'New feedstock system for fused filament fabrication of sintered alumina parts', *Materials*, 13(19), pp. 1–12. Available at: https://doi.org/10.3390/ma13194461.

Onagoruwa, S., Bose, S. and Bandyopadhyay, A. (2001) 'Fused deposition of ceramics (FDC) and composites', *Proceedings of Solid Freeform Fabrication Symposium*, pp. 224–231. Available at: http://edge.rit.edu/edge/P10551/public/SFF/SFF 2001 Proceedings/2001 SFF Papers/26-Onagoruwa.pdf.

Orlovská, M. *et al.* (2020) 'Fracture and mechanical properties of lightweight alumina ceramics prepared by fused filament fabrication', *Journal of the European Ceramic Society*, 40(14), pp. 4837–4843. Available at: https://doi.org/10.1016/j.jeurceramsoc.2020.02.026.

Patel, S.B. *et al.* (2017) 'Transparent TiO2 nanotubes on zirconia for biomedical applications', *RSC Advances*, 7(48), pp. 30397–30410. Available at: https://doi.org/10.1039/c7ra03940a.

Schlichting, K.W., Padture, N.P. and Klemens, P.G. (2001) 'Thermal conductivity of dense and porous yttria-stabilized zirconia', *Journal of Materials Science*, 36(12), pp. 3003–3010. Available at: https://doi.org/10.1023/A:1017970924312.

Serdeczny, M.P. *et al.* (2018) 'Experimental validation of a numerical model for the strand shape in material extrusion additive manufacturing', *Additive Manufacturing*, 24(June), pp. 145–153. Available at: https://doi.org/10.1016/j.addma.2018.09.022.

Spina, R. (2019) 'Performance analysis of colored PLA products with a fused filament fabrication process', *Polymers*, 11(12). Available at: https://doi.org/10.3390/polym11121984.

Sthle, L. and Wold, S. (1989) 'Analysis of variance (ANOVA)', *Chemometrics and Intelligent Laboratory Systems*, 6(4), pp. 259–272. Available at: https://doi.org/10.1016/0169-7439(89)80095-4.

Thomas-vielma, P., Cervera, A. and Levenfeld, B. (2008) 'Production of alumina parts by powder injection molding with a binder system based on high density polyethylene', 28, pp. 763–771. Available at: https://doi.org/10.1016/j.jeurceramsoc.2007.08.004.

Tong, H. *et al.* (2016) 'Characterization of three commercial Y-TZP ceramics produced for their High-Translucency, High-Strength and High-Surface Area', *Ceramics International*, 42(1), pp. 1077–1085. Available at: https://doi.org/10.1016/j.ceramint.2015.09.033.

Willems, E. *et al.* (2021) 'Additive manufacturing of zirconia ceramics by material jetting', *Journal of the European Ceramic Society*, 41(10), pp. 5292–5306. Available at: https://doi.org/10.1016/j.jeurceramsoc.2021.04.018.

Wright, J.K. *et al.* (1990) 'Particle Packing in Ceramic Injection Molding', *Journal of the American Ceramic Society*, V, pp. 2653–2658.

Yves-Christian, H. *et al.* (2010) 'Net shaped high performance oxide ceramic parts by Selective Laser Melting', *Physics Procedia*, 5(PART 2), pp. 587–594. Available at: https://doi.org/10.1016/j.phpro.2010.08.086.

Zeng, Y. *et al.* (2022) 'Effect of different sintering additives type on Vat photopolymerization 3D printing of Al 2 O 3 ceramics', *Journal of Manufacturing Processes*, 83(June), pp. 414–426. Available at: https://doi.org/10.1016/j.jmapro.2022.09.022.

Material extrusion additive manufacturing of zirconia: from filament characterisation to Weibull statistics

Abstract

Purpose - This research aims to investigate the performance of filament-based Material Extrusion additive manufacturing (MEX), combined with debinding and sintering as a novel approach to manufacturing ceramic components.

Design/methodology/approach - A commercial ZrO_2 filament was selected and analysed by IR spectroscopy, rheology and thermo-gravimetry. The influence of the print parameters (layer thickness, flow rate multiplier, printing speed) and sintering cycle were investigated to define a suitable printing and sintering strategy. Biaxial flexure tests were applied on sintered discs realised with optimised printing strategies and the results were analysed via Weibull statistics to evaluate the mechanical properties of printed components. The hardness and thermal conductivity of sintered components were also tested.

Findings – Layer thickness and flow rate multiplier of the printing process were proved to have significant effect on the density of as-printed parts. Optimised samples display a sintered density > 99% of the theoretical density, 20% linear sintering shrinkage, a characteristic flexural strength of 871 MPa with a Weibull modulus of 4.9, a Vickers hardness of 12.90 ± 0.3 GPa and a thermal conductivity of 3.62 W/mK. Gyroids were printed for demonstration purposes.

Originality/value – This work is the first to apply biaxial flexure tests and Weibull statistics to additively manufactured MEX zirconia components, hence providing comparable results to other additive technologies. Moreover, fractography analysis builds the connection between printing defects and the fracture mechanism of bending. This study also provides guidelines for fabricating high density zirconia components with MEX.

Keywords: Additive manufacturing, Material extrusion, Ceramic, Weibull statistics, Fracture analysis

1. Introduction

Technical ceramics are widely applied in multiple domains, such as aerospace and electronics, as they are excellent thermal and electrical insulators. However, due to their low

fracture toughness, ceramic component manufacturing is a labour and cost intensive process. It mostly relies on near-net-shape techniques, such as uniaxial pressing and injection moulding, and it is limited in geometrical shape and has high mould investment costs. Additive Manufacturing (AM) can however overcome these limitations.

Different AM technologies have been launched to process ceramics. Selective laser melting (SLM) is capable of processing pure ceramic powder above the melting temperature. This approach allows direct manufacturing of ceramics with high density (approx. 100%) at the cost of high investment and required preheating to avoid thermal warping (Yves-Christian *et al.*, 2010). Selective laser sintering (SLS), as a similar but indirect approach, applies a composite powder composed of ceramic and a secondary component as the binder (e.g. polymer/inorganic compound), yet fine mixing of the composite powder remains the major barrier of SLS (Chen *et al.*, 2018). Two other prominent AM technologies for ceramics: stereolithography (SLA) and material jetting (MJ) both utilise UV-curable resin and confer high density and strength to the fabricated final components (Nakai *et al.*, 2021; Willems *et al.*, 2021; Zeng *et al.*, 2022). On the other hand, the drawbacks of using ceramic slurry in SLA and MJ consist in the environmental impact of the toxic photo resin and limited choice of materials (Gibson and Rosen, no date).

Among various AM technologies, filament-based Material Extrusion additive manufacturing (MEX) (ISO/ASTM 52900) is one of the most widely utilised technologies to produce polymeric parts, due to the limited hardware investment and user-friendly printer setup. Apart from polymer printing, MEX has expanded to fibre-reinforced polymers, metals, and ceramics (Chen *et al.*, 2019; Galantucci *et al.*, 2019).

A MEX filament for ceramic part production typically consists of 45-55 vol% nanometric ceramic powders with a binder system acting as the backbone, tackifier, and plasticiser. The ceramic filament is heated to 160 - 265 °C (Nötzel *et al.*, 2021) in the extruding nozzle to obtain a low-viscosity melt that can be extruded and deposited. The as-printed part (green part) is subjected to one thermal or multiple (catalytic or solvent + thermal) debinding steps to remove most of the binder system, leaving a porous ceramic part with low organic binder content, referred to as the brown part. The brown part is then thermally debound and sintered to obtain dense ceramic components (Ferraris *et al.*, 2016). Additional machining processes can be applied to the green or sintered objects to reach a higher accuracy and surface finish. The introduction of the binders in MEX drastically lowers the required investment cost for AM of

ceramic and reduces potential hazards for users by avoiding directly operating with nanoparticles. The necessary post processes are accompanied by a longer production period and energy consumption, nevertheless, MEX achieves good cost-effectiveness compared to other AM technologies

Research on MEX of ceramics is still in an early stage. The available reports typically focus on a particular aspect, such as feedstock development or manufacturing feasibility in a trial-and-error approach. As an example, Onagoruwa et al. conducted extensive research on the employable binders and their functions as backbone, elastomer, tackifier, and plasticiser, and applied a polypropylene-based feedstock to produce mullite, fused silica, and titanium oxide-based filament feedstocks (Onagoruwa, Bose and Bandyopadhyay, 2001). Nötzel et al. developed a alumina filament using polyvinyl butyral and polyethylene glycol as binders, and reached a sintered relative density of 98% (Nötzel and Hanemann, 2020). Cano et al. studied the effect of the applied infill pattern during MEX on the flexural strength of sintered zirconia parts via 3-point bending. The parts with alternating +/- 45° infill direction had a final density of 97% and a characteristic flexural strength of 500 MPa with a Weibull modulus of 6.5 (Cano *et al.*, 2020). However, the studies are very fragmented and typically focused on a particular step of the process or part performance.

This work systematically investigates the MEX process of ceramics along the entire process chain including feedstock inspection, printing optimisation, two-step debinding, sintering, and sintered components characterisation. A 3Y-TZP zirconia grade was selected and studied due to its high strength potential and phase transformation induced fracture toughness attributed to the 3 mol% yttria stabiliser content. The density, Vickers hardness, thermal conductivity, and biaxial strength of the sintered zirconia parts were characterised and accompanied by a detailed fracture analysis. For the first time, biaxial flexure test was adopted to assess the mechanical performance of MEX fabricated zirconia part. This research further demonstrates the capability of filament-based material extrusion additive manufacturing to manufacture ceramic parts of satisfactory mechanical performance at limited costs.

2. Materials and Methods

2.1 Feedstock Materials

A 3 mol% yttria-stabilised zirconia (3Y-TZP) filament with a diameter of 1.75 mm was purchased from 3DCeram Sinto Tiwari GmbH (Germany). Amongst the commercially available filaments, only solutions involving chemical and/or thermal debinding with low

toxicity were considered for the sake of low environmental impact and reduced hazard. The diameter distribution of the filament was inspected with a laser diameter gauge (DGK2015, Proton Products) to ensure accurate material feeding during printing. Fourier transformed infra-red spectroscopy (FT/IR-4200, Jasco Co.), was used for the binder characterisation in the ATR mode with a resolution of 4 cm^{-1}. Several FT-IR-ATR measurements were done at arbitrary points on each sample, and an average spectrum was computed. Thermo-gravimetric analysis (TGA) and differential scanning calorimetry (DSC) were performed (SDT Q600, TA Instruments) on the filament at a constant heating rate of 10 °C/min up to 1000 °C in pure Ar gas (Liquid Argon > 99.998%, $O_2 \leq 1.5$ ppm, Nippon Gases NV) to assist defining suitable thermal debinding and sintering strategies.

Rheology parameters of the material in the green state were measured using a rotational rheometer (Haake Mars III, Thermo Scientific) in parallel plate geometry. Specifically, plates of 20 mm diameter were adopted, and experiments were conducted at 180 °C under controlled shear rate conditions between 1 and 300 s^{-1} to emulate the rheological conditions during printing and achieve adequate torque values. All measurements were repeated five times and were performed in air. No thermal degradation was detected during the tests. Under these experimental conditions, the morphology of the polymer suspension was stable, as verified before and after measurements. Cross-sections of the filament were inspected by optical microscopy (K6000, Keyence) and scanning electron microscopy (SEM, Vega3 LMH, Tescan).

2.2 3D Printing

Different from thermoplastics, printing was performed on a Prusa i3 MK3s particularly with direct drive configuration which stably feeds the brittle filament without breaking. To ensure smooth extrusion, 0.4 mm was selected as the nozzle diameter as it is over 10 times bigger than the particle size of the studied zirconia in this research. Besides, a hardened steel nozzle was used to avoid abrasion. Screening experiments were conducted to identify a suitable process window. Accordingly, the following print parameters were maintained constant during sample production: nozzle temperature 180 °C, bed temperature 60 °C, fan cooling on at 25% from the 5^{th} layer, strand width 0.4 mm, double contour, and 100% infill with alternating +/- 45° patterns; whereas a full factorial design of experiments (DoE, see Table I, 3 repetitions per experiments) was applied to investigate the main and interaction effects of the layer thickness, printing speed and flow rate multiplier on the green printed density of 10×10×5 mm^3 prismatic parts.

Table I: Full factorial design of experiments.

Factors	level 1	level 2	level 3
Printing speed (mm/s)	10	30	50
Layer thickness (mm)	0.1	0.2	0.3
Flow rate multiplier	90%	100%	110%

2.3 Post Processing

Post-processing, successively in the form of: i) solvent debinding, ii) thermal debinding, and iii) pressureless sintering was applied to selected printed samples, and combined with suitable print parameters towards the establishment of best-practice manufacturing strategies. Post-processing was developed based on the results of the TGA analyses, and dedicated tests conducted internally. Accordingly, the parts were immersed in a magnetically stirred acetone bath for 48 h during solvent debinding, at a temperature 40 °C to accelerate the process and avoid cracking. The solvent was replaced with fresh acetone after 24 h. Afterwards, the parts remained in open air for 12 h to allow evaporation of the residual acetone. The total weight loss after solvent debinding was 8.6%. The open porosity generated during binder dissolution allows a higher heating rate during the subsequent thermal debinding process, without the risk of cracking the part due to severe gas release.

Thermal debinding of the remaining binder occurred in a muffle furnace in air (Carbolite, model RHF 1200). The parts were initially heated to 150 °C at 1.3 °C/min and dwelled for 1 h. After that, the parts were heated from 150 °C to 450 °C with a heating rate of 0.5 °C/min and dwelled for 1 h. Cooling was performed at 5 °C/min to room temperature. The weight loss by thermal debinding was 5.7%. The applied solvent temperature, heating rates, dwelling times, and 2-step debinding strategy accomplished a good balance between process time and defect free parts (Thomas-vielma, Cervera and Levenfeld, 2008). Finally, the parts were sintered in air (Nabertherm HT16/17) by heating to 1000 °C at 4 °C/min and to 1475 °C at 2 °C/min with a dwell time of 2 h.

2.4 Characterisation

The Archimedes method (ISO 18754:2020) was selected to measure the actual volumetric density (g/cm^3) due to its high accuracy in comparison to cross-section microscopy and micro-CT. The density of the filament, as well as green and sintered parts was measured in ethanol using an analytical balance (Quintix 224-1S, Sartorius). Microstructural analyses were performed by Scanning Electron Microscopy (SEM, XL30FEG, FEI) on mirror-polished and

platinum-coated cross-sectioned sintered parts. Biaxial flexure test (ISO 6872:2015) was selected due to the larger sample volume tested in tension compared to 3-point bending testing and the available literature references for comparison (Miura *et al.*, 2020). Accordingly, two populations of 30 disc samples with a thickness of 1.2 mm and a diameter of 14 mm were manufactured with the best-practice manufacturing strategy for mechanical testing. A 20% disc oversize was set during printing to compensate for sintering shrinkage, grinding, and polishing, required during sample preparation. The biaxial flexure test were performed on an Instron 5567 with a crosshead speed of 1 mm/s. The strength data were analysed by Weibull statistics, allowing to quantify the characteristic strength, i.e. the strength at which 63.2% of the samples fracture, and the Weibull modulus, which quantifies the strength distribution. The fracture surfaces were characterised by SEM (nanoSEM, FEI) after gold coating. The Vickers hardness (H_V) of polished prismatic parts, produced by the best-practice manufacturing strategy, was measured (Model FV700, Future Tech Corp, Tokyo, Japan) using a load of 98 N applied for 10 s. Five indentations were made on each part. In addition, thermal conductivity at room temperature was measured on cylinders (D24.3 mm × 2.1 mm) of one of the best-practice manufacturing strategies, using a Modified Transient Plane Source (MTPS) (ASTM D7984) single-sided sensor (Trident, C-Therm Technologies Ltd, Fredericton, Canada). Complex gyroids were manufactured for demonstrative purposes.

3. Experimental results and discussion

3.1 Feedstock Characterisation

The as-supplied filament diameter was measured to be 1.753 ± 0.004 mm. Correspondingly, the measured distribution (given in Figure 1a) forms a nearly normal distribution with $\sigma = 0.0042$ and $\mu = 1.753$. The high accuracy of the filament allowed for not only a stable material flow into the extruder, but also continuous friction between the feeding rollers and the

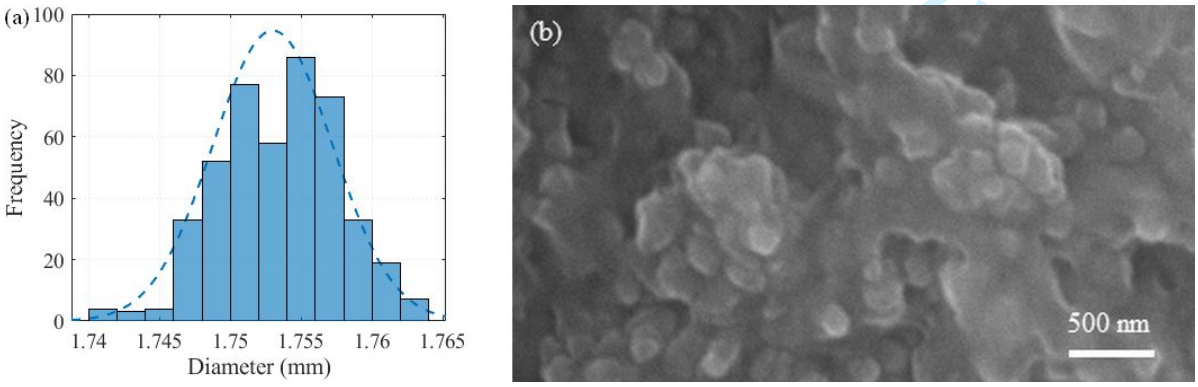

Figure 1: (a) Histogram of the measured diameter distribution of the zirconia filament; (b) SEM picture of a cross-sectional area of the zirconia filament.

filament creating constant pressure inside the nozzle. SEM inspection of cross-sections of the filament reveals zirconia particles in the nanometre range (Figure 1b).

The absorbance FT-IR spectrum of the zirconia-based filament shows prominent peaks at 2912 and 2848 cm^{-1} which allowed to identify polyethylene as the primary polymer in the filament (Figure 2). An additional peak was associated with primary aliphatic amine at 3397 cm^{-1}. The characteristic peaks of the zirconia particles were located in the 900 and 500 cm^{-1} range (Patel *et al.*, 2017). Based on the TGA results (Figure 3 (a)), a total weight loss of 14.49% was measured, indicating a powder load of 85.51 wt.% in the feedstock, equivalent to 50 vol.% given the average density of polymeric binders. Moreover, the presence of three types of binders in different proportions can be distinguished with onset decomposition temperatures of 170 °C, 385 °C, and > 500 °C, respectively. An endothermic peak at 55.1 °C in the DSC curve (Figure 3a) indicates the melting process of a binder, which is believed to be paraffin wax (Giavarini, C. Pochetti, 1973; Jayalakshmi *et al.*, 2007; Nötzel and Hanemann, 2020). Most of the weight loss occurs in the range of 150 °C - 450 °C, which is later defined as the temperature for thermal debinding. The total weight loss of 14.49% equals the one registered after solvent and thermal debinding (see sect. 2.3).

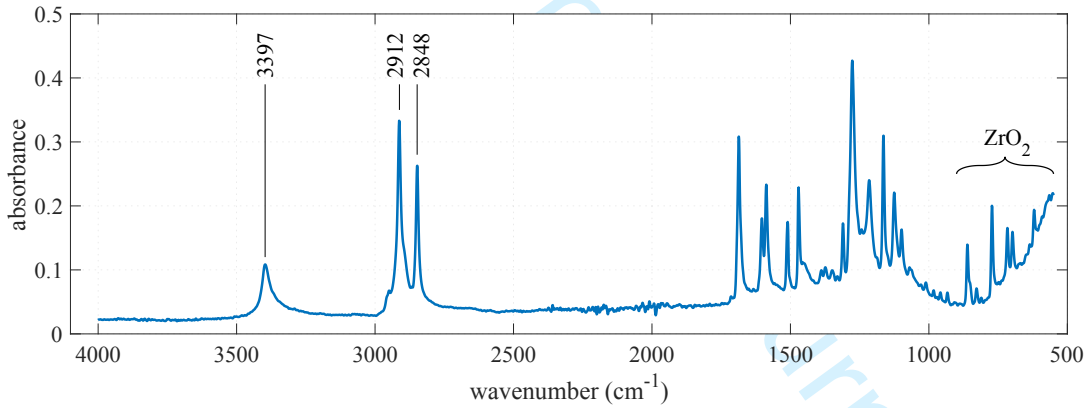

Figure 2: FT-IR spectrum of the as-purchased zirconia filament.

According to the rheological data (Figure 3b), the viscosity rapidly drops eight orders of magnitude from the lowest to the highest shear regime, reaching an infinite-shear viscosity of 5×10^{-4} Pa·s at 102 s^{-1}, which corresponds to the shear rate applied during printing (shear rates under printing > 102 s^{-1}). When compared with typical MEX filament polymeric data (in-house measurements and literature data (Spina, 2019)), this infinite-shear viscosity is particularly low, most likely due to the proper binder system allowing to well-disperse the nanometric zirconia particles.

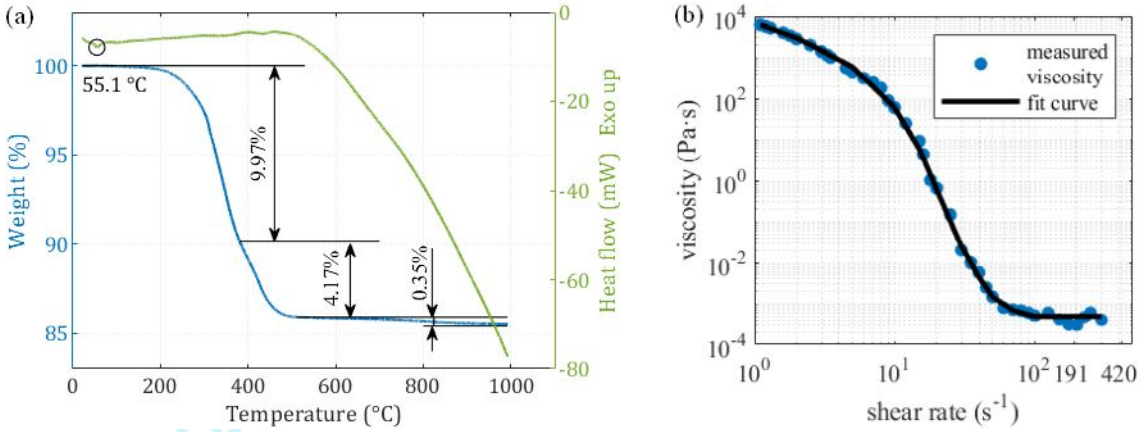

Figure 3: (a) TGA (blue) and DSC (green) curve of the zirconia filament; (b) viscosity of the feedstock melt at 180 °C as a function of shear rate and its spline fit curve.

3.2 3D Printing

Figure 4 provides a colour map of the relative green density of ZrO_2 printed samples as a function of the flow rate multiplier and layer thickness for a representative printing speed of 30 mm/s. An increase in the flow rate multiplier and a decrease of the layer thickness favour high density printed parts; and relative green densities > 98% are easily achievable with a flow rate multiplier > 100%, regardless of the other parameters. The Analysis of variance (ANOVA) was utilised to analyse the effect of each tested printing parameter and their interactions on the green density. Accordingly, the green density data were tested against the F-distribution, and the corresponding p-values (that is the area under the F-distribution from the given F-values to the end of the distribution tail) were calculated. Notably, a p-value below the widely accepted benchmark of 0.05 indicates that the associated factor has a significant effect on the target parameter of the ANOVA (Sthle and Wold, 1989). Statistically, the flow rate multiplier is the most significant factor, followed by the layer thickness and their interaction, while the significance of the printing speed is negligible (Table II). The regression model's coefficient (R^2) is 0.91. Those identified trends well agree with the general understanding of the MEX process using filament feedstock. A high flow rate multiplier induces over-extrusion of material, which is beneficial to fill the gaps of printing, especially in the case of low viscous melts. This contribution is even more important when printing with high layer thickness (or more properly with layer thickness closer to the nozzle diameter) because of the larger porosity of the printed part as a result of the deposition of strands with almost circular cross sections. On the contrary, a lower layer thickness as compared to the nozzle diameter is, to a certain extent, in favour of a flat strand deposition, with almost rectangular cross-sectional profiles, which minimises the

gap across adjacent strands and overlapping layers, hence the printed part porosity (Serdeczny *et al.*, 2018). The negligibility of the printing speed can also be attributed to the low viscosity of the feedstock used.

Table II: Results of the Analysis of Variance (ANOVA) of the effect of printing factors on the green part densities.

Source	**Sum Sq.**	***p*-value**
Layer thickness	0.02892	2.83×1^{-6}
Printing speed	0.00156	4.30×10^{-1}
Flow rate multiplier	0.43473	8.41×10^{-30}
Layer thickness * printing speed	0.00485	2.70×10^{-1}
Layer thickness * flow rate multiplier	0.03315	7.87×10^{-6}
Printing speed * flow rate multiplier	0.00286	5.42×10^{-1}
Error	0.05669	
Total	0.56726	

The prismatic samples printed at 30 mm/s were then selected for post-printing processing via solvent, thermal debinding, and sintering, as from the post-processing protocol described in sect.2. Accordingly, two best-practice manufacturing strategies, as summarised in

Table III, could be identified. They were characterised by a green relative density > 98% and a sintered relative density > 99%; and they were further applied for sample and biaxial flexural disc production. The physical and mechanical characteristics of the sintered samples are summarised in Table IV and further discussed in the next section.

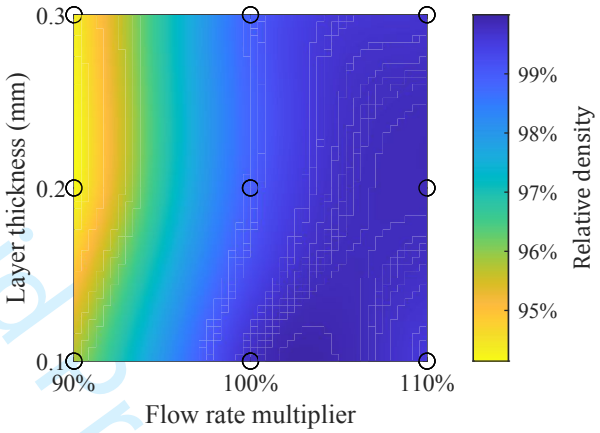

Figure 4: Color map of relative densities of zirconia printed green samples as a function of flow rate multiplier and layer thickness at a representative printing speed of 30 mm/s (interpolated data). The circles represent the location of the experimental data points.

Table III: Best-practice manufacturing strategies.

	01_100_30	**02_110_30**
Layer thickness (mm)	0.1	0.2
Flow rate multiplier	100%	110%
Printing speed (mm/s)	30	30
Green relative density[2]	98.87±0.03%	98.84±0.02%
Sintered relative density[3]	99.99±0.14%	99.38±0.06%

[2]Normalised to the density of the zirconia filament, 3.55 g/cm^3

[3]Normalised to the theoretical density of zirconia (3Y-TZP), 6.05 g/cm^3 (Tong *et al.*, 2016)

3.3 Characterisation of Sintered Parts

Figure 5 shows BSE images of representative cross-sections of sintered prismatic parts realised via best-practice manufacturing strategies 01_100_30 (a) and 02_110_30 (b). As shown, the cross-sections reveal a nearly fully dense microstructure with few aligned and randomly distributed pores. Particularly, elongated and layer-aligned residual pores with a maximum length of 60 µm and 120 µm, were detected in the cross-sections of 01_100_30 and 02_110_30 parts, respectively. The presence of pores can either be attributed to the inhomogeneity of the material feedstock, the inclusion of air bubbles in the low viscous melt, or printing defects. The larger flaw size of the 02_110_30 samples can be related to the higher printing layer thickness resulting in a larger inter-strand space.

The measured Vickers hardness was similar for both manufacturing strategies, and showed good consistency with zirconia parts fabricated via conventionally sintering (Cokic *et al.*, 2020) and material jetting (Willems *et al.*, 2021), while the flexural strength was substantially different. Table IV listed the results on hardness, thermal and mechanical properties of zirconia in this study and other references. The discs printed with printing strategy 01_100_30 had a Weibull modulus of 2.66 and a characteristic strength of 730 MPa, whereas the 02_110_30 strategy resulted in a higher Weibull modulus of 4.91 and characteristic strength of 871 MPa. The Weibull plots of both populations are compared in Figure 6, along with characteristic pictures of two fractured discs. Low-strength discs typically broke in 2 parts, while discs with a strength above 1000 MPa broke in 5 or 6 parts. The higher Weibull modulus obtained with the 02_110_30 strategy should be ascribed to the double printing layer thickness applied, implying printing half the number of layers and a reduced probability of inducing printing defects in comparison to the 01_100_30 strategy. The obtained characteristic flexural strength is superior to 508 MPa for MEX with a different printing strategy (Cano *et al.*, 2020), and it is comparable to the reported 702 MPa for conventional ceramic processing (Cokic *et al.*, 2020)

and other additively manufacturing technologies, such as 741 MPa for stereolithography (Lu *et al.*, 2020) and 1061 MPa for material jetting (Willems *et al.*, 2021). However, the Weibull modulus remains modest compared to the above-mentioned studies which range from 6.5 to 16.3, most likely due to the higher intrinsic defect-inducing nature of the MEX process using filament feedstock.

Table IV: Mechanical and thermal characteristics of 3Y-TZP discs and samples realised with best-practice manufacturing strategies in this study and other references using the same grade of zirconia.

Manufacturing method	**MEX 01_100_30**	**MEX 02_110_30**	**MEX**	**Speed Sintering**	**SLA**	**Material Jetting**
Vickers hardness (GPa)	12.98±0.03	12.90±0.33	/	13.1	/	12.8
Weibull modulus	2.66	4.91	6.5	6.3	8.7	8.5
Characteristic strength (MPa)	730	871	508	702	741.8	1061
Thermal conductivity (W/mK)	/	3.62±0.08	/	/	/	/
Bending test	biaxial	biaxial	3-point	biaxial	3-point	biaxial
Source	this study	this study	(Cano *et al.*, 2020)	(Cokic *et al.*, 2020)	(Lu *et al.*, 2020)	(Willems *et al.*, 2021)

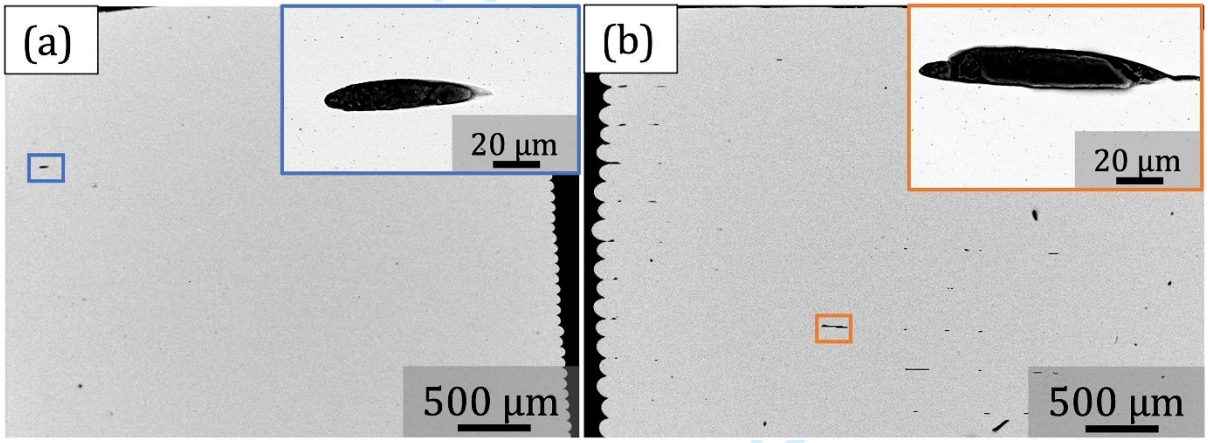

Figure 5: Backscattered Electron (BSE) images of representative cross-sections of sintered prismatic parts realised via best-practice manufacturing strategies 01_100_30 (a) and 02_110_30 (b).

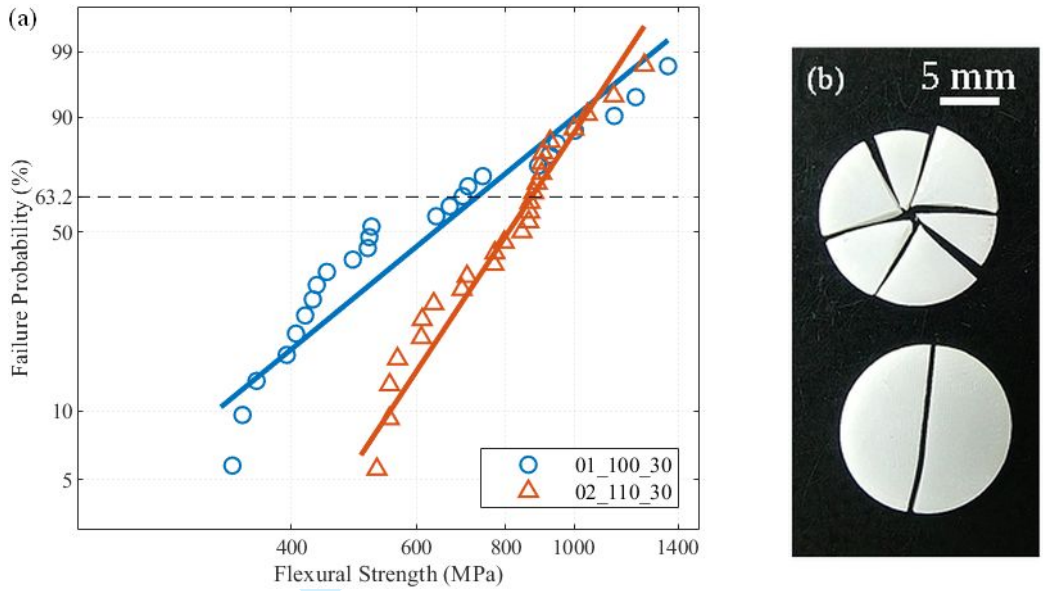

Figure 6: (a) Weibull plot of the biaxial flexural strength of 3Y-TZP discs (population 01_100_30 and 02_110_30) and (b) fractured discs after mechanical testing (right: bottom = low strength, top = high strength).

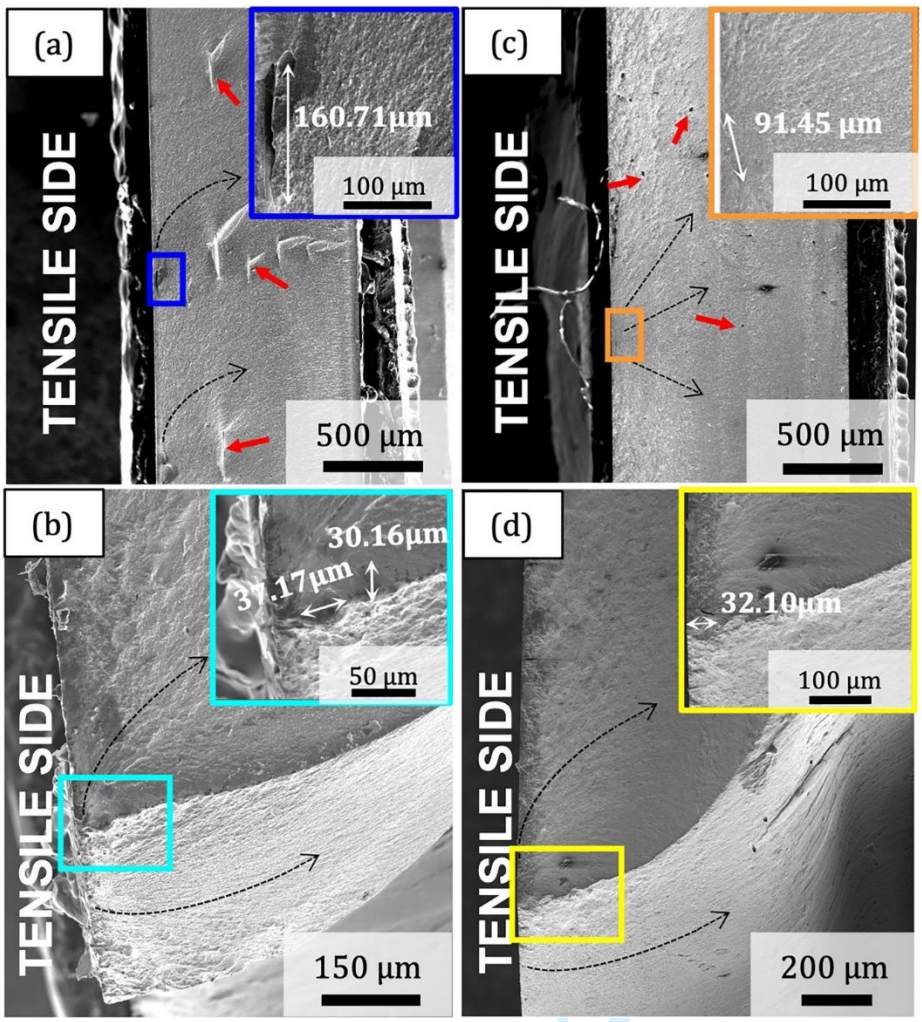

Figure 7: Secondary electron (SE) images of the biaxial fracture surface of 3Y-TZP discs manufactured by MEX using printing strategy 01 100 30 (a,b) and 02 110 30 (c,d). Indicative measurements of the critical flaw size.

The fractography analysis of a selection of biaxially fractured discs is shown in Figure 7. Two 01_100_30 discs with a flexural strength of 630 MPa (Figure 7a) and 1130 MPa (Figure 7b) and two 02_110_30 discs with the same flexural strength of 630 MPa (Figure 7c) and 1130 MPa (Figure 7d) were analysed. The dashed black arrows show the crack propagation direction observed on the fracture surface starting from the identified critical flaws. The crack initiation points were mainly investigated on the flat surfaces subjected to tensile stresses during testing where the crack propagation pattern appeared to originate from. For the low strength 01_100_30 part (Figure 7a), a possible crack initiation point was identified as an elongated void of ~160 µm in length and parallel to the printing direction as shown in the magnified

image (blue box in Figure 7a). Several defects with the same morphology (indicated by the red arrows) were observed over the complete fracture surface and were attributed to interlayer defects. On the contrary, for the low strength 02_110_30 part (Figure 7c), the critical flaw was identified as a smaller nearly spherical defect measured to be ~90 μm in diameter (as shown in the orange box in Figure 7c). Similar spherical isolated pores (pointed by the red arrows) were detected on the fracture surface as well. The significant variation in the morphology, size and amount of the voids between the low strength 01_100_30 and 02_110_30 parts did not account for any difference in their final strength. This discrepancy highlights that the position and orientation play a major role in the resulting mechanical properties compared to the percentage and distribution of defects. Despite the smaller size and aspect ratio of the porosity in the 02_110_30 part, the presence of a defect near the tensile surface determined the failure of the part at low stress values. On the other hand, being the orientation of the voids parallel to the tensile surface the 01_100_30 part resulted in the same value of strength. Since the part was tested in the favourable direction, the anisotropy generated through the layer-by-layer printing had a relatively limited impact on the mechanical properties in this case. For the high-strength parts, the fracture surface was analysed at low (Figure 7b-d) and high magnification (light blue and yellow box). The former highlighted the direction of the crack, whereas the latter enabled quantifying the size of the pores from which the crack initiated. In both cases, the critical defects are spherical in nature and of similar size. The formation of spherical pores could be correlated to air bubbles or ZrO_2 particle-free polymer agglomerates in the filament.

Strategy 02_110_30 was finally selected to fabricate cylinders for thermal characterisation too. The measured thermal conductivity was reported to be 3.62±0.08 W/mK at room temperature (Table IV), which is in good agreement with the reported value of 3.2 W/mK for conventionally pressed and sintered fully dense 3Y-TZP (Schlichting, Padture and Klemens, 2001), and slightly higher than the 2.99 W/mK reported for the same zirconia grade manufactured via stereolithography and sintered at 1600 °C (Liu *et al.*, 2023).

The printability and effect of the printing parameters were substantially related to the feedstock properties, such as binder properties, melt viscosity, particle size distribution, etc. A feedstock with comparable above-mentioned properties is essential to reproduce dense green parts using the printing strategy acquired in this study. Subsequently, the composite green parts underwent debinding and sintering and evolved into a monolithic ceramic. Similar conditions (temperature, heating ramp and dwelling time) as in this study or milder modifications of them facilitate defect-free binder removal and nearly full densification. In particular, the powder load

of the feedstock is a critical factor for densification during sintering. Using a filament with 43 vol.% powder, Guan et al. reported MEX fabricated zirconia with a relative density over of 99% after sintering, while an abrupt density drop occurred with a powder load below this threshold (Guan *et al.*, 2023). Therefore, a feedstock with a powder load above 43 vol.% (and ideally close to 50 vol.%) is regarded as a requirement to reproduce the results of this study.

3.4 Gyroid demonstrator

Gyroid parts (green size 30×30×7 mm^3) were printed as a benchmark piece demonstrating the shaping capability offered by the MEX technology (Figure 8). A linear sintering shrinkage of 18% was measured in X, Y and Z directions, which is in line with the level of shrinkage measured on the prismatic parts during the experimental campaign (19.89±0.62%). The shrinkage value is in good consistent with the linear shrinkage of ceramic via MEX and injection moulding in other researches - between 18% to 21% (Wright *et al.*, 1990; Cano *et al.*, 2020; Orlovská *et al.*, 2020; Nötzel *et al.*, 2021), and higher than the 5-11% via conventional firing (Correia, Hotza and Segadães, 2004). Defects like cracks, warpage or distortion were not observed on the sintered part, validating good geometry retention of the complex part containing overhanging and thin-wall structures during the sintering process. Hence, the isotropic linear shrinkage and fine geometry retention facilitate the application of this technology in industry.

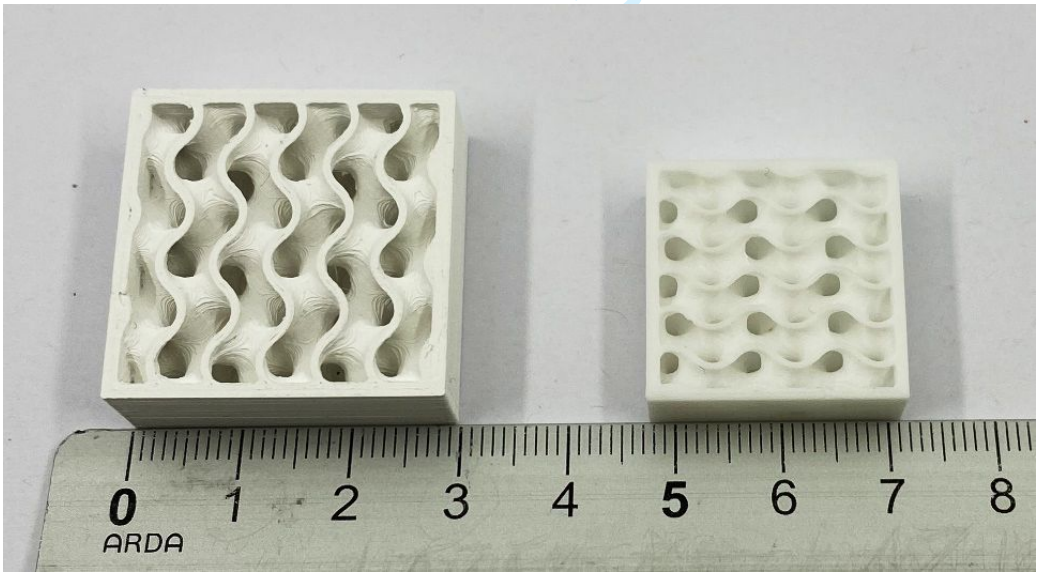

Figure 8: Green (left) and sintered (right) zirconia gyroid.

4. Conclusions

Material extrusion-based additive manufacturing using ceramic filament feedstock was proven to be capable of printing highly dense zirconia. Following conclusions were derived:

- DoE and ANOVA analyses of the printing parameters indicated that the layer thickness and flow rate multiplier significantly influence the as-printed green density. The printing strategy based on the statistical approach gave a sintered relative density >99%. This outcome can be extrapolated to other ceramic feedstocks with comparable particle size and morphology to fabricate dense parts via Material Extrusion with not only filament feedstock but also granulates, paste, etc..
- Satisfactory mechanical properties (Vickers hardness of 12.90 GPa, characteristic flexural strength up to 871 MPa and Weibull modulus of 4.9) were attained with the best-practice printing strategies. Analysis of the fractured surfaces revealed critical defects of variable size (indicatively in the range of 30 to 160 μm) of both spherical and elongated nature, attributed to inhomogeneities in the filament and inter-filament spacing printing defects, respectively.
- The sintered zirconia exhibited a thermal conductivity of 3.62 W/mK, a typical value for a dense 3Y-TZP ceramic, which is a thermal insulator.
- The sintered gyroid structure demonstrated homogeneous shrinkage and good geometry integrity after sintering. With the freedom of design due to additive manufacturing, zirconia serves as a good candidate for electrical and thermal insulation material.

The adoption of a commercially available filament introduced advantages in dimensional accuracy and printability. However, the unknown binder formulation forms a black box for processing. Under this circumstance, an exemplary strategy incorporating printing parameters, debinding conditions and sintering conditions was formulated in this study based on the extensive filament characterisation and the design of experiments on printing parameters to acquire defect-free zirconia components with high density and good mechanical properties. Details on the binder formulation would provide a reference from the material's perspective, which allows cross-validation between the experimentally formulated processing strategy of the whole process chain and the intrinsic property of the binders.

This study elucidates the impact of the printing parameters on the density of as-printed zirconia parts via Material Extrusion, and evaluated the mechanical and thermal properties of sintered specimens fabricated with the selected printing strategy. Future research will focus on the direct effect of printing strategy on mechanical property to further improve the reliability and strength of the material.

Acknowledgments

The authors acknowledge Frederik Desplentere for support in the filament diameter characterisation. The authors thank Prof. Luigi Galantucci of Politecnico di Bari for his precious suggestions and support. Part of this work is conducted in the framework of the SBO-FWO project Multi-Material Additive Manufacturing for Electrical Machines with increased performance (AM4EM, S001721N), funded by FWO-Vlaanderen.

References

Cano, S. *et al.* (2020) 'Influence of the infill orientation on the properties of zirconia parts produced by fused filament fabrication', *Materials*, 13(14). Available at: https://doi.org/10.3390/ma13143158.

Chen, A. *et al.* (2018) 'High-performance ceramic parts with complex shape prepared by selective laser sintering : a review', 6753. Available at: https://doi.org/10.1080/17436753.2017.1379586.

Chen, Z. *et al.* (2019) '3D printing of ceramics: A review', *Journal of the European Ceramic Society*, 39(4), pp. 661–687. Available at: https://doi.org/10.1016/j.jeurceramsoc.2018.11.013.

Cokic, S.M. *et al.* (2020) 'Mechanical properties, aging stability and translucency of speed-sintered zirconia for chairside restorations', *Dental Materials*, 36(7), pp. 959–972. Available at: https://doi.org/10.1016/j.dental.2020.04.026.

Correia, S.L., Hotza, D. and Segadães, A.M. (2004) 'Simultaneous optimization of linear firing shrinkage and water absorption of triaxial ceramic bodies using experiments design', *Ceramics International*, 30, pp. 917–922. Available at: https://doi.org/10.1016/j.ceramint.2003.10.013.

Ferraris, E. *et al.* (2016) 'Shaping of engineering ceramics by electro, chemical and physical processes', *CIRP Annals - Manufacturing Technology*, 65(2), pp. 761–784. Available at: https://doi.org/10.1016/j.cirp.2016.06.001.

Galantucci, L.M. *et al.* (2019) *Additive Manufacturing: New Trends in the 4th Industrial Revolution*, *Lecture Notes in Mechanical Engineering*. Springer International Publishing. Available at: https://doi.org/10.1007/978-3-030-18180-2_12.

Giavarini, C. Pochetti, F. (1973) 'Characterization of petroleum products by DSC analysis', *Journal of Thermal Analysis*, 5, pp. 83–94.

Gibson, I. and Rosen, D. (no date) *Additive Manufacturing Technologies*.

Guan, Z. *et al.* (2023) 'Additive manufacturing of zirconia ceramic by fused filament fabrication', *Ceramics International*, 49(17), pp. 27742–27749. Available at: https://doi.org/10.1016/j.ceramint.2023.05.230.

Jayalakshmi, V. *et al.* (2007) 'Characterisation of paraffin waxes by DSC and high temperature GC', *Petroleum Science and Technology*, 6466(May). Available at: https://doi.org/10.1080/10916469908949752.

Liu, Yansong *et al.* (2023) 'Influence of sintering temperature on the thermal conductivity of digital light processing 3D-printed yttria-stabilized zirconia ceramic', *Ceramics International*, 49(16), pp. 27514–27525. Available at: https://doi.org/10.1016/j.ceramint.2023.06.027.

Lu, Y. *et al.* (2020) 'Journal of the European Ceramic Society Flexural strength and Weibull analysis of Y-TZP fabricated by stereolithographic additive manufacturing and subtractive manufacturing', *Journal of the European Ceramic Society*, 40(3), pp. 826–834. Available at: https://doi.org/10.1016/j.jeurceramsoc.2019.10.058.

Miura, D. *et al.* (2020) 'Reliability of different bending test methods for dental press ceramics', *Materials*, 13(22), pp. 1–10. Available at: https://doi.org/10.3390/ma13225162.

Nakai, H. *et al.* (2021) 'Additively manufactured zirconia for dental applications', *Materials*, 14(13), pp. 1–9. Available at: https://doi.org/10.3390/ma14133694.

Nötzel, D. *et al.* (2021) 'Printing of zirconia parts via fused filament fabrication', *Materials*, 14(19). Available at: https://doi.org/10.3390/ma14195467.

Nötzel, D. and Hanemann, T. (2020) 'New feedstock system for fused filament fabrication of sintered alumina parts', *Materials*, 13(19), pp. 1–12. Available at: https://doi.org/10.3390/ma13194461.

Onagoruwa, S., Bose, S. and Bandyopadhyay, A. (2001) 'Fused deposition of ceramics (FDC) and composites', *Proceedings of Solid Freeform Fabrication Symposium*, pp. 224–231. Available at: http://edge.rit.edu/edge/P10551/public/SFF/SFF 2001 Proceedings/2001 SFF Papers/26-Onagoruwa.pdf.

Orlovská, M. *et al.* (2020) 'Fracture and mechanical properties of lightweight alumina ceramics prepared by fused filament fabrication', *Journal of the European Ceramic Society*, 40(14), pp. 4837–4843. Available at: https://doi.org/10.1016/j.jeurceramsoc.2020.02.026.

Patel, S.B. *et al.* (2017) 'Transparent TiO2 nanotubes on zirconia for biomedical applications', *RSC Advances*, 7(48), pp. 30397–30410. Available at: https://doi.org/10.1039/c7ra03940a.

Schlichting, K.W., Padture, N.P. and Klemens, P.G. (2001) 'Thermal conductivity of dense and porous yttria-stabilized zirconia', *Journal of Materials Science*, 36(12), pp. 3003–3010. Available at: https://doi.org/10.1023/A:1017970924312.

Serdeczny, M.P. *et al.* (2018) 'Experimental validation of a numerical model for the strand shape in material extrusion additive manufacturing', *Additive Manufacturing*, 24(June), pp. 145–153. Available at: https://doi.org/10.1016/j.addma.2018.09.022.

Spina, R. (2019) 'Performance analysis of colored PLA products with a fused filament fabrication process', *Polymers*, 11(12). Available at: https://doi.org/10.3390/polym11121984.

Sthle, L. and Wold, S. (1989) 'Analysis of variance (ANOVA)', *Chemometrics and Intelligent Laboratory Systems*, 6(4), pp. 259–272. Available at: https://doi.org/10.1016/0169-7439(89)80095-4.

Thomas-vielma, P., Cervera, A. and Levenfeld, B. (2008) 'Production of alumina parts by powder injection molding with a binder system based on high density polyethylene', 28, pp. 763–771. Available at: https://doi.org/10.1016/j.jeurceramsoc.2007.08.004.

Tong, H. *et al.* (2016) 'Characterization of three commercial Y-TZP ceramics produced for their High-Translucency, High-Strength and High-Surface Area', *Ceramics International*, 42(1), pp. 1077–1085. Available at: https://doi.org/10.1016/j.ceramint.2015.09.033.

Willems, E. *et al.* (2021) 'Additive manufacturing of zirconia ceramics by material jetting', *Journal of the European Ceramic Society*, 41(10), pp. 5292–5306. Available at: https://doi.org/10.1016/j.jeurceramsoc.2021.04.018.

Wright, J.K. *et al.* (1990) 'Particle Packing in Ceramic Injection Molding', *Journal of the American Ceramic Society*, V, pp. 2653–2658.

Yves-Christian, H. *et al.* (2010) 'Net shaped high performance oxide ceramic parts by Selective Laser Melting', *Physics Procedia*, 5(PART 2), pp. 587–594. Available at: https://doi.org/10.1016/j.phpro.2010.08.086.

Zeng, Y. *et al.* (2022) 'Effect of different sintering additives type on Vat photopolymerization 3D printing of Al 2 O 3 ceramics', *Journal of Manufacturing Processes*, 83(June), pp. 414–426. Available at: https://doi.org/10.1016/j.jmapro.2022.09.022.

Table I: Full factorial design of experiments.

Factors	**level 1**	**level 2**	**level 3**
Printing speed (mm/s)	10	30	50
Layer thickness (mm)	0.1	0.2	0.3
Flow rate multiplier	90%	100%	110%

Table I: Results of the Analysis of Variance (ANOVA) of the effect of printing factors on the green part densities.

Source	**Sum Sq.**	***p*-value**
Layer thickness	0.02892	2.83×1^{-6}
Printing speed	0.00156	4.30×10^{-1}
Flow rate multiplier	0.43473	8.41×10^{-30}
Layer thickness * printing speed	0.00485	2.70×10^{-1}
Layer thickness * flow rate multiplier	0.03315	7.87×10^{-6}
Printing speed * flow rate multiplier	0.00286	5.42×10^{-1}
Error	0.05669	
Total	0.56726	

Table I: Best-practice manufacturing strategies.

	01_100_30	**02_110_30**
Layer thickness (mm)	0.1	0.2
Flow rate multiplier	100%	110%
Printing speed (mm/s)	30	30
Green relative density[2]	98.87±0.03%	98.84±0.02%
Sintered relative density[3]	99.99±0.14%	99.38±0.06%

[2]Normalised to the density of the zirconia filament, 3.55 g/cm^3

[3]Normalised to the theoretical density of zirconia (3Y-TZP), 6.05 g/cm^3 (Tong *et al.*, 2016)

Table I: Mechanical and thermal characteristics of 3Y-TZP discs and samples realised with best-practice manufacturing strategies in this study and other references using the same grade of zirconia.

Manufacturing method	**MEX 01_100_30**	**MEX 02_110_30**	**MEX**	**Speed Sintering**	**SLA**	**Material Jetting**
Vickers hardness (GPa)	12.98±0.03	12.90±0.33	/	13.1	/	12.8
Weibull modulus	2.66	4.91	6.5	6.3	8.7	8.5
Characteristic strength (MPa)	730	871	508	702	741.8	1061
Thermal conductivity (W/mK)	/	3.62±0.08	/	/	/	/
Bending test	biaxial	biaxial	3-point	biaxial	3-point	biaxial
Source	this study	this study	(Cano *et al.*, 2020)	(Cokic *et al.*, 2020)	(Lu *et al.*, 2020)	(Willems *et al.*, 2021)

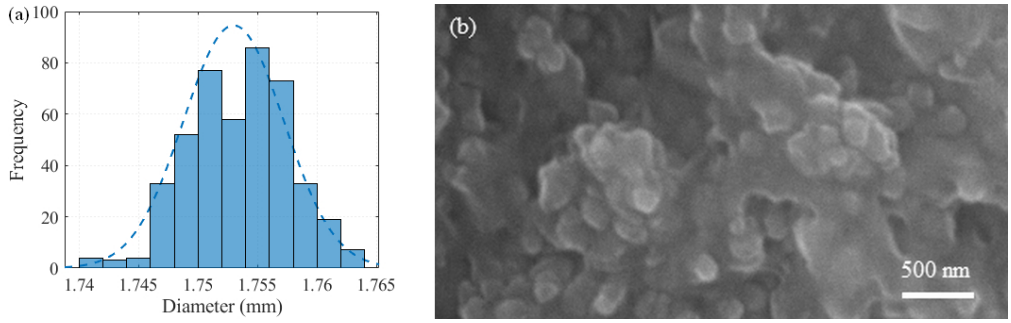

Figure 1: (a) Histogram of the measured diameter distribution of the zirconia filament; (b) SEM picture of a cross-sectional area of the zirconia filament.

179x56mm (150 x 150 DPI)

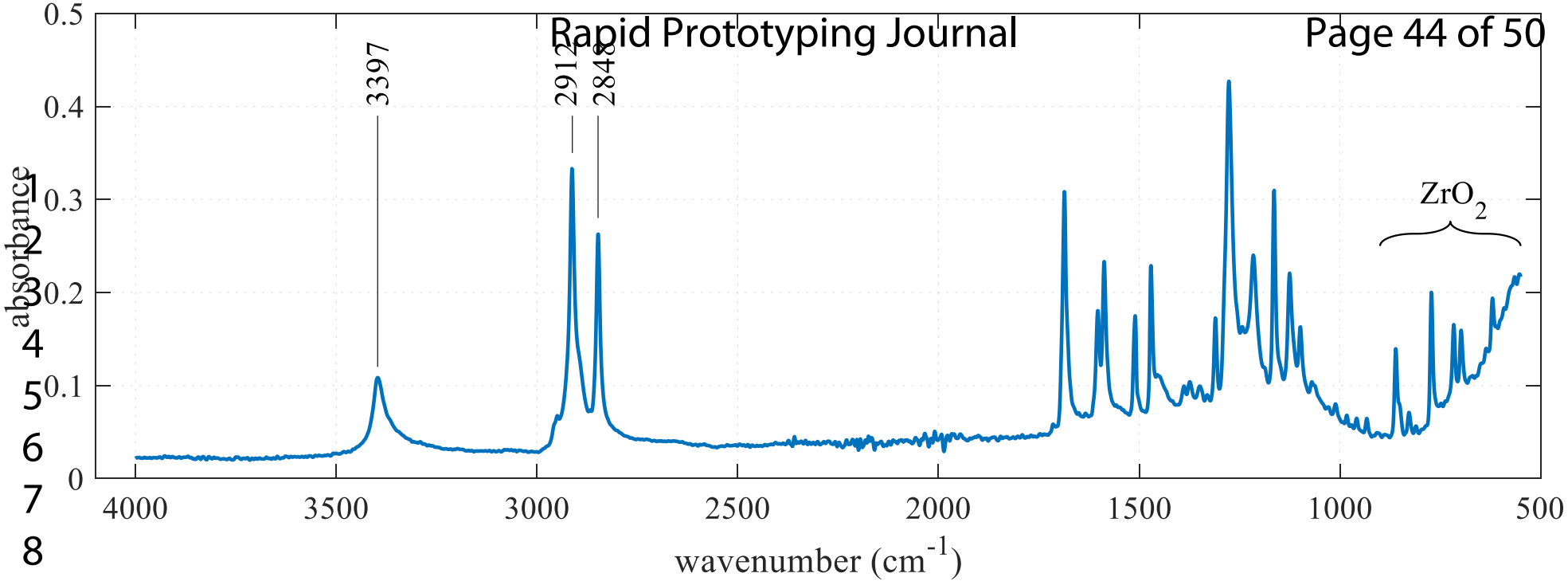
absorbance
wavenumber (cm-1)
3397
2912
2848
ZrO2
0.5
0.4
0.3
0.2
0.1
0
4000
3500
3000
2500
2000
1500
1000
500

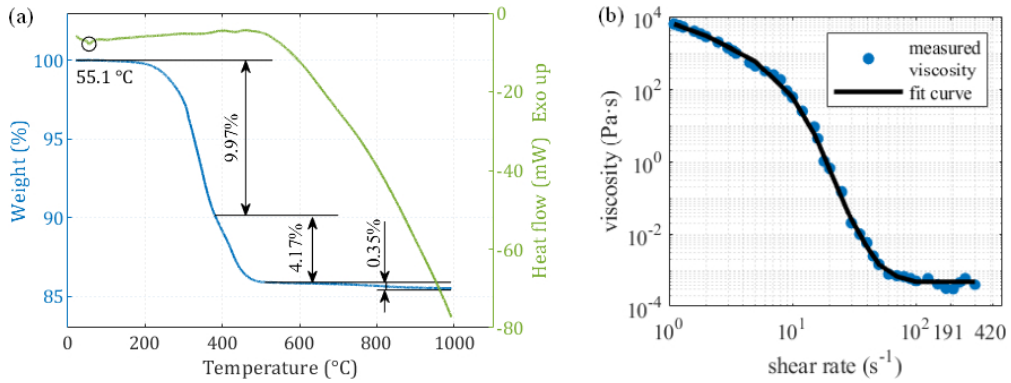

Figure 3: (a) TGA (blue) and DSC (green) curve of the zirconia filament; (b) viscosity of the feedstock melt at 180 °C as a function of shear rate and its spline fit curve.

149x56mm (150 x 150 DPI)

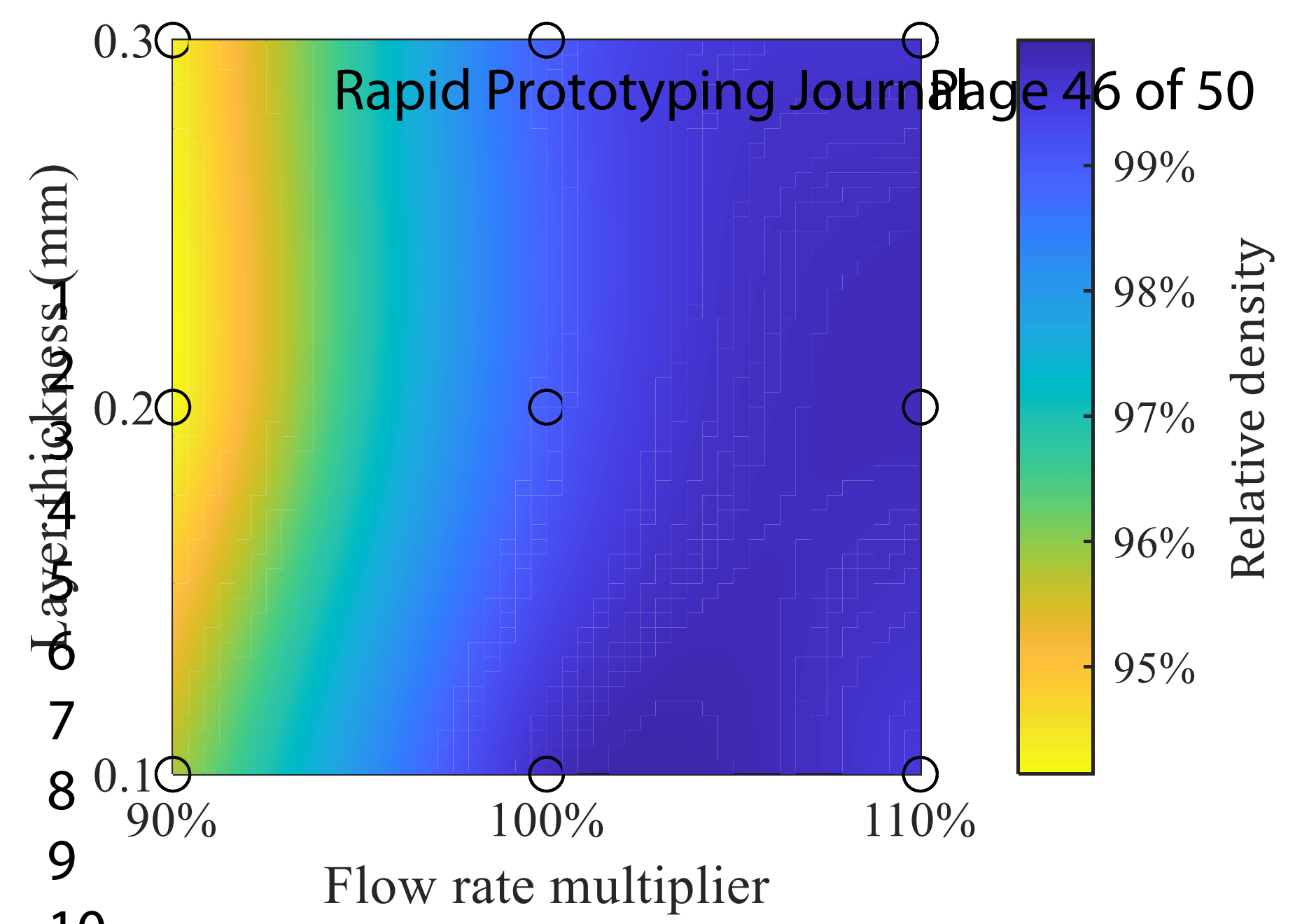
0.3
0.2
0.1
Layer thickness (mm)
90%
100%
110%
Flow rate multiplier
99%
98%
97%
96%
95%
Relative density

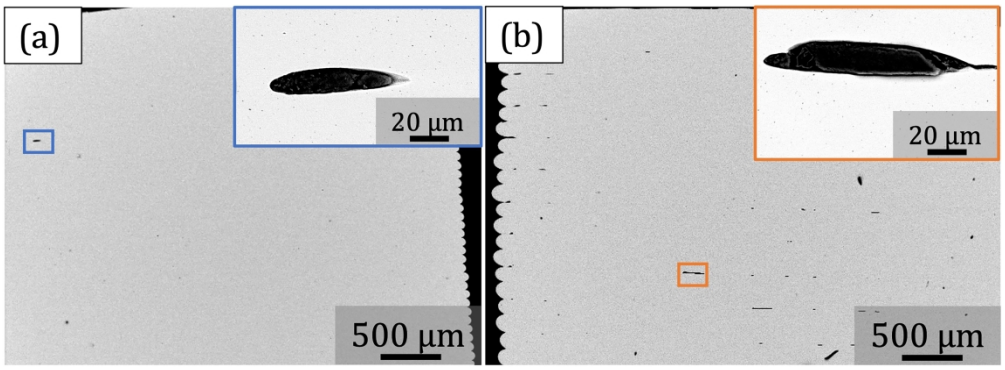

Figure 5: Backscattered Electron (BSE) images of representative cross-sections of sintered prismatic parts realized via best-practice manufacturing strategies 01_100_30 (a) and 02_110_30 (b).

996x362mm (120 x 120 DPI)

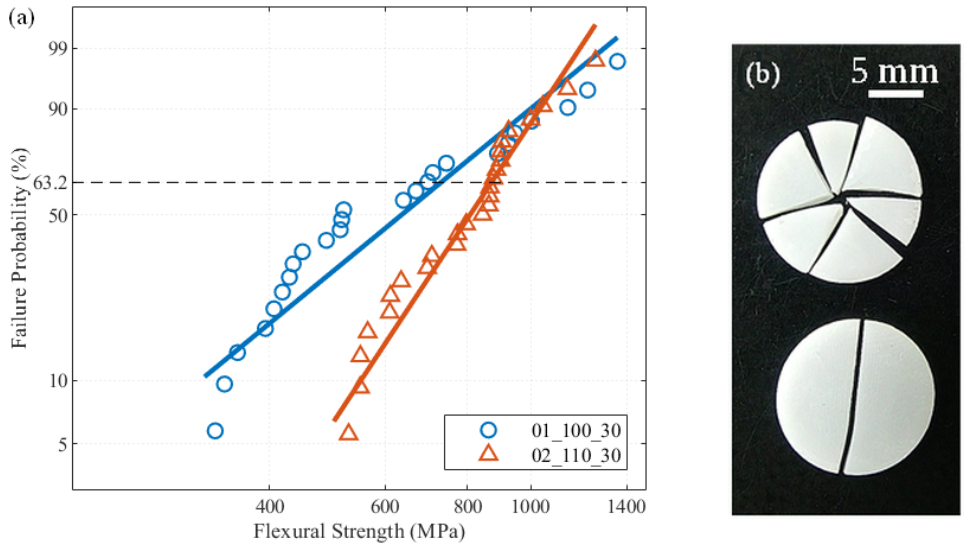

Figure 6: (a) Weibull plot of the biaxial flexural strength of 3Y-TZP discs (population 01_100_30 and 02_110_30) and (b) fractured discs after mechanical testing (right: bottom = low strength, top = high strength).

142x77mm (150 x 150 DPI)

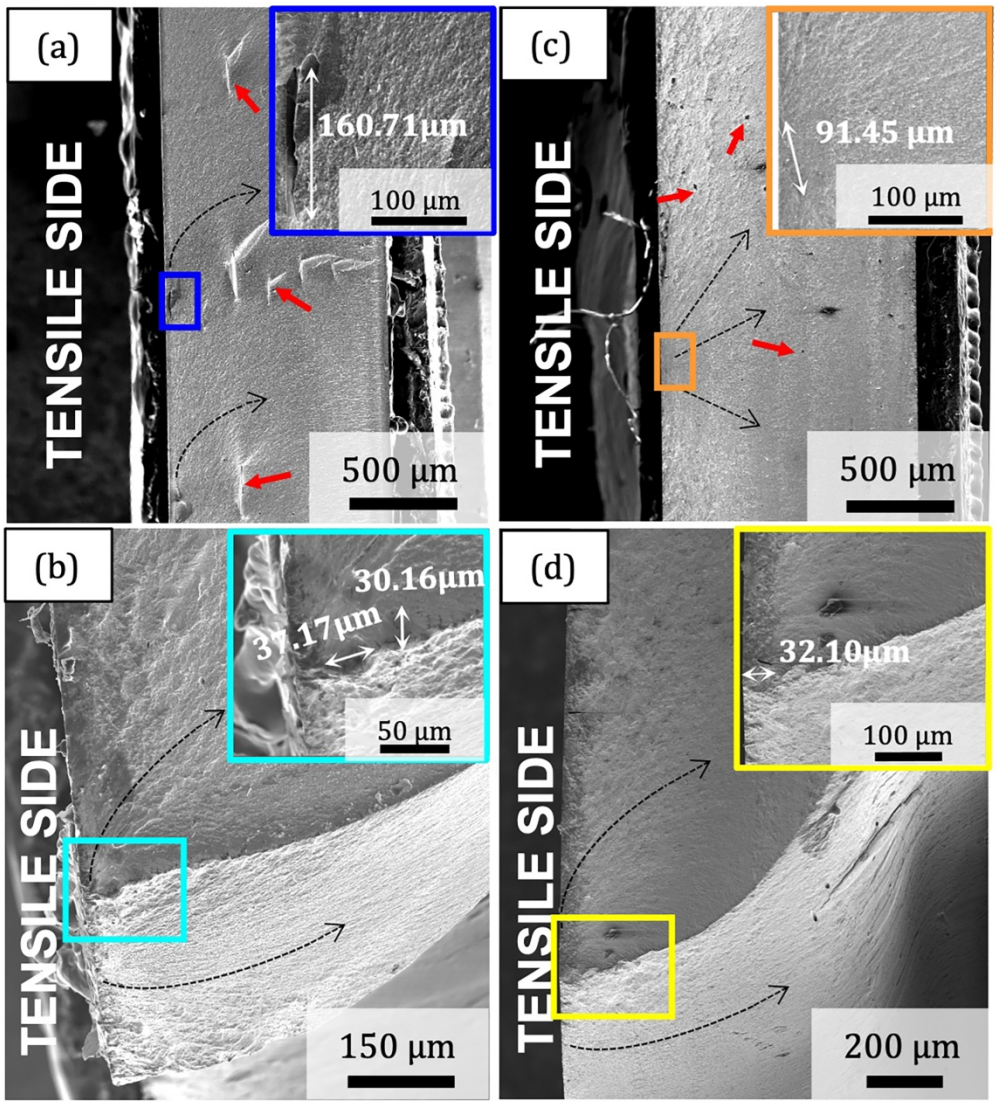

Figure 7: Secondary electron (SE) images of the biaxial fracture surface of 3Y-TZP discs manufactured by MEX using printing strategy 01 100 30 (a,b) and 02 110 30 (c,d). Indicative measurements of the critical flaw size.

483x531mm (120 x 120 DPI)

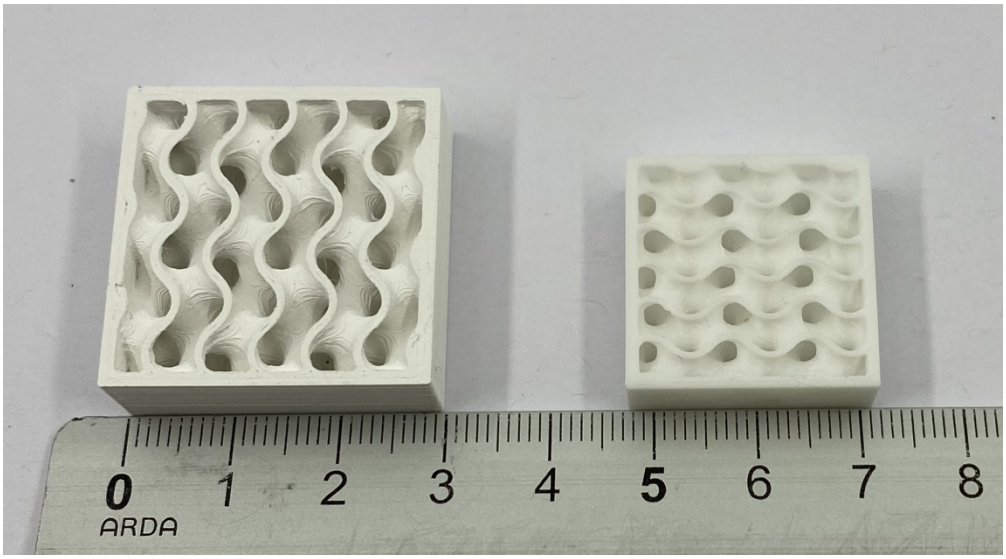

Figure 8: Green (left) and sintered (right) zirconia gyroid.

406x223mm (120 x 120 DPI)